

**THREE DIMENSIONAL SIMULATION OF
FLUID STRUCTURE INTERACTIONS FOR
RED BLOOD CELLS**

M.Sc. THESIS

Ayşe ÇETİN

Department of Aeronautical and Astronautical Engineering

Aeronautical and Astronautical Engineering Programme

JUNE

**THREE DIMENSIONAL SIMULATION OF
FLUID STRUCTURE INTERACTIONS FOR
RED BLOOD CELLS**

M.Sc. THESIS

**Ayşe ÇETİN
(511161108)**

Department of Aeronautical and Astronautical Engineering

Aeronautical and Astronautical Engineering Programme

Thesis Advisor: Prof. Dr. Mehmet ŞAHİN

JUNE

**KIRMIZI KAN HÜCRELERİ İÇİN ÜÇ BOYUTLU
AKIŞKAN YAPI ETKİLEŞİMİ SİMÜLASYONU**

YÜKSEK LİSANS TEZİ

**Ayşe ÇETİN
(511161108)**

Uçak ve Uzay Mühendisliği Anabilim Dalı

Uçak ve Uzay Mühendisliği Programı

Tez Danışmanı: Prof. Dr. Mehmet ŞAHİN

2018

Ayşe ÇETİN, a M.Sc. student of ITU Graduate School of Science Engineering and Technology 511161108 successfully defended the thesis entitled “THREE DIMENSIONAL SIMULATION OF FLUID STRUCTURE INTERACTIONS FOR RED BLOOD CELLS”, which she prepared after fulfilling the requirements specified in the associated legislations, before the jury whose signatures are below.

Thesis Advisor : **Prof. Dr. Mehmet ŞAHİN**
Istanbul Technical University

Jury Members : **Asst. Prof. Dr. Bayram ÇELİK**
Istanbul Technical University

Assoc. Prof. Dr. Kerem PEKKAN
Koc University

.....

Date of Submission : **04 May 2018**

Date of Defense : **07 June 2018**





To my family,



FOREWORD

First and foremost, my deepest appreciation goes to my supervisor Prof. Dr. Mehmet Şahin for his inestimable support, encouragement, guidance, and patience. Without his guidance and support, this project would not be completed. I will never forget the opportunities he has given to me, which are the most valuable ones throughout my educational life. I am really grateful for studying under his guidance.

My special thanks goes to my dear friends Baki Şervan Bozkuş, Nazmi Erdi Coşkunpınar, Altun Rzayev and all members of HEMLAB for helping me survive all the stress from this year and not letting me give up. I owe them a debt of gratitude for their precious friendship. Thanks to my family for their consistent love, support and efforts they have put into raising and shaping me.

I would like to acknowledge the use of the computing resources provided by the National Center for High Performance Computing of Turkey (UYBHM) under grant number 10752009 and the computing facilities at TUBITAK-ULAKBIM, High Performance and Grid Computing Center.

June

Ayşe ÇETİN
(M.Sc.)

TABLE OF CONTENTS

	<u>Page</u>
FOREWORD	ix
TABLE OF CONTENTS	xi
ABBREVIATIONS	xiii
SYMBOLS	xv
LIST OF TABLES	xvii
LIST OF FIGURES	xix
SUMMARY	xxiii
ÖZET	xxv
1. INTRODUCTION	1
1.1 Purpose of Thesis	1
1.2 Literature Review	3
1.3 Outline	8
2. GOVERNING EQUATIONS	11
2.1 Fluid Equations.....	11
2.2 Solid Equations.....	11
2.3 Interface Conditions	12
2.4 Fully Coupled Solver.....	12
3. DESCRIPTION OF THE PROBLEM	17
3.1 Red Blood Cell Geometry	17
3.2 Boundary Conditions.....	18
4. TWO-DIMENSIONAL NUMERICAL RESULTS	21
4.1 Convergence Studies.....	22
4.2 Single Red Blood Cell in a Channel with Different Height	24
4.3 Multiple Red Blood Cells in a Channel with a Height of 15.6μm	27
5. THREE-DIMENSIONAL NUMERICAL RESULTS	31
6. CONCLUSION	45
REFERENCES	47
CURRICULUM VITAE	53



ABBREVIATIONS

ALE	: Arbitrary Lagrangian-Eulerian
BDF2	: Second-Order Backward Difference
CFD	: Computational Fluid Dynamics
CSD	: Computational Structural Dynamics
DGCL	: Discrete Geometric Conservation Law
DOF	: Degree of Freedom
DPD	: Dissipative Particle Dynamics
FGMRES	: Flexible Generalized Minimal Residuals
FSI	: Fluid Structure Interaction
IFEM	: Immersed Finite Element Method
ILU	: Incomplete Lower-Upper
M	: Mesh i.e. M1, M2, M3
NS	: Navier-Stokes
PETSc	: Parallel Extensible Toolkit for Scientific Computing
pIBM	: penalty Immersed Boundary Method
PMIS	: Parallel Modified Independent Set
RBC	: Red Blood Cell
RBF	: Radial Basis Function
SL	: Spectrin-Link
SPH	: Smoothed Particle Hydrodynamics
WBC	: White Blood Cell



SYMBOLS

\mathbf{d}	: Displacement vector
D	: Diameter of RBC
E	: Elasticity module
\mathbf{E}	: Green-Lagrangian strain tensor
\mathbf{F}	: Deformation gradient tensor
h	: Inward thickness of RBC
n	: Normal vector
p	: Fluid pressure
\mathbf{u}	: Local fluid velocity vector
Ω	: Arbitrary moving control volume
\dot{x}	: Grid velocity
μ_f	: Fluid dynamic viscosity
ρ_s	: Solid material density per unit undeformed volume
ρ_f	: Fluid constant density
σ_s	: Cauchy stress tensor
σ_f	: Fluid stress tensor
Π	: Non-symmetric first Piola
R_0	: Initial radius of RBC
λ_s	: Material Lamé's constant
ν_s	: Poison ratio
$T(r)$: Thickness of RBC in the x -direction
$()^\top$: Transpose
U_{max}	: Maximum inflow velocity



LIST OF TABLES

	<u>Page</u>
Table 3.1 : Physical parameters for red blood cell and fluid plasma (<i>pg</i> : picogram).	18
Table 4.1 : Computational meshes used for simulation of red blood cell for a channel height of $15.6\mu m$	22
Table 5.1 : Computational meshes used for simulation of red blood cell for a channel height of $15.6\mu m$	31





LIST OF FIGURES

	<u>Page</u>
Figure 1.1 : Illustration of red blood cells (RBCs) (or erythrocytes), white blood cells (WBCs) (or leukocytes), and platelets (or thrombocytes).	1
Figure 1.2 : Apparent viscosity of blood as a function of shear rates [a] and hematocrit effects on blood as a function of shear rates [b].	2
Figure 1.3 : Human red blood cells flowing in glass tubes.	3
Figure 1.4 : Mathematical FSI domain.	5
Figure 3.1 : Geometry of red blood cell.	17
Figure 3.2 : Physical boundary conditions for a single red blood cell in a capillary tube.	19
Figure 4.1 : Computational two-dimensional coarse mesh M1 [a], medium mesh M2 [b] and fine mesh M3 [c] for a single red blood cell in a channel with a height of $15.6\mu m$.	23
Figure 4.2 : Spatial convergence with $\Delta t = 100\mu s$ [a] and temporal convergence on mesh M2 [b] for a single red blood cell in a channel with a height of $15.6\mu m$ at $t = 60ms$.	23
Figure 4.3 : Effect of different membrane thickness h using same shear modulus μ_s [a] and same membrane shear modulus $\mu_s h$ [b] to final red cell geometry at $t = 60ms$ in a channel with a height of $15.6\mu m$ at $t = 60ms$ on mesh M3.	24
Figure 4.4 : Final positions/deformations at $t = 60ms$ with computed u -velocity component contours and velocity profiles at several different locations for a single red cell in a channel with a height of $15.6\mu m$ [a], $11.7\mu m$ [b] and $10\mu m$ [c] on mesh M3.	25
Figure 4.5 : Velocity profiles at $x = 40.0\mu m$ and the location corresponding to maximum red cell diameter at $t = 60ms$ in a channel with a height of $15.6\mu m$ [a], $11.7\mu m$ [b] and $10\mu m$ [c] on mesh M3.	25
Figure 4.6 : Single red blood cell. Red blood cell positions/deformations at several different time levels for a channel height of $15.6\mu m$ [a], $11.7\mu m$ [b] and $10\mu m$ [c] on mesh M3.	26
Figure 4.7 : Comparison of red blood cell deformations at several different time levels ($\Delta t = 5ms$) for a channel height of $15.6\mu m$ [a] and comparison of final cell geometry with results for several different channel heights at $t = 60ms$ [b] on mesh M3.	27
Figure 4.8 : Final positions/deformations at $t = 60ms$ with computed u -velocity component contours for 5 cells [a] and 9 cells [b] in a channel with a height of $15.6\mu m$ on mesh M3.	28

Figure 4.9 :	Comparison of wall vorticity divided by the wall vorticity of planar Poiseuille flow for five and nine cells for a channel height of $15.6\mu m$ [a] and comparison of fluid pressure along the capillary channel symmetry line for different hematocrit ratios and capillary channel heights [b] at $t = 60ms$ on mesh M3.	29
Figure 5.1 :	Partial view of computational three-dimensional coarse mesh M1 with 93,840 nodes and 88,331 hexahedral elements for a single red blood cell in a capillary tube with a diameter of $15.6\mu m$	31
Figure 5.2 :	Red blood cell positions/deformations with computed u -velocity component contours at $z = 0$ plane at $t = 60ms$ for a capillary tube diameter of $15.6\mu m$ [a], $11.7\mu m$ [b] and $10\mu m$ [c] on mesh M1.	32
Figure 5.3 :	Velocity profiles at $x = 30.0\mu m$ and the location corresponding to maximum red cell diameter at $t = 60ms$ in a channel with a height of $15.6\mu m$ [a], $11.7\mu m$ [b] and $10\mu m$ [c] on mesh M1.	32
Figure 5.4 :	Red blood cell positions/deformations at several different time levels for a single red blood cell in a capillary tube with a diameter of $15.6\mu m$ [a], $11.7\mu m$ [b] and $10\mu m$ [c] on mesh M1.	33
Figure 5.5 :	Red blood cell positions/deformations at several different time levels for a single red blood cell in a capillary tube with a diameter of $15.6\mu m$ [a], $11.7\mu m$ [b] and $10\mu m$ [c] on mesh M1.	34
Figure 5.6 :	Time-variation of red blood cell deformations at $z = 0$ plane at several different time levels ($\Delta t = 10ms$) [a], comparison of final cell geometry at $t = 60ms$ for several different tube diameters [b] on mesh M1.	36
Figure 5.7 :	Comparison of deformations in two- and three-dimensions at $t = 60ms$ for a channel height/tube diameter of $15.6\mu m$ [c] on mesh M1.	37
Figure 5.8 :	Mesh convergence of cupcake shaped membrane buckling instability on mesh M1 [a], mesh M2 [b] and mesh M3 [c] for a capillary tube diameter of $10\mu m$ at $t = 60ms$	38
Figure 5.9 :	Time evolution of cupcake shaped membrane buckling instability on mesh M3 at $t = 20ms$ [a], $t = 40ms$ [b] and $t = 60ms$ [c] for a capillary tube diameter of $10\mu m$	38
Figure 5.10 :	Front [a] and back [b] views of wall shear stress vectors and their streamtraces along with pressure contours for a capillary tube diameter of $10.0\mu m$ at $t = 60ms$ on mesh M1.	39
Figure 5.11 :	Effect of initial orientation on red cell positions/deformations at several different time levels for a single red blood cell in a capillary tube with a diameter of $10\mu m$ [c] on mesh M1.	40
Figure 5.12 :	Effects of hematocrit density using five red cells [a] and nine red cells [b] on u -velocity on $z = 0$ plane and deformations for a capillary tube diameter of $15.6\mu m$ at $t = 60ms$ on mesh M1.	41
Figure 5.13 :	Comparison of three-dimensional red cell membrane geometry corresponding to maximum indentation [a] and protrusion [b] with the results of Zhao et al. [4] and Shi et al. [5] for a capillary tube diameter of $9.024\mu m$ at $t = 60ms$	42

Figure 5.14: Effect of computational mesh to development of buckling for a capillary tube diameter of $9.024\mu m$ at $t = 40ms$: Initial unstructured mesh M1 [a] and partially axisymmetric mesh M1 [b]. 43





THREE DIMENSIONAL SIMULATION OF FLUID STRUCTURE INTERACTIONS FOR RED BLOOD CELLS

SUMMARY

Red blood cells, also called erythrocytes, can be defined as nucleus-free deformable liquid capsules enclosed by a biological membrane that is nearly incompressible and exhibits a viscoelastic response to shearing and bending deformation. The mechanical properties of red cells strongly influence the rheological behavior of blood and introduce non-Newtonian effects. A number of human diseases such as hypertension, malaria, sickle cell anemia and diabetes mellitus leads to change in the mechanical properties of red blood cells and reduction in deformability, which increase in microvascular flow resistance and a decrease in cellular oxygen delivery.

A parallel fully-coupled (monolithic) fluid-structure interaction (FSI) algorithm has been applied to the deformation of red blood cells (RBCs) in capillaries, where cell deformability has significant effects on blood rheology. In the present FSI algorithm, fluid domain is discretized using the side-centered unstructured finite volume method based on Arbitrary Lagrangian-Eulerian (ALE) formulation, meanwhile solid domain is discretized with the classical Galerkin finite element formulation for the Saint Venant-Kirchhoff material in a Lagrangian frame. In addition, the compatible kinematic boundary condition is enforced at the interface between the solid and fluid domains in order to satisfy the global discrete geometric conservation law (DGCL), which is important in order to conserve the mass of cytoplasmic fluid within the red cell at machine precision. In order to solve the resulting large-scale algebraic linear systems in a fully coupled (monolithic) manner, a new matrix factorization is introduced similar to that of the projection method and the parallel algebraic multigrid solver BoomerAMG is used for the scaled discrete Laplacian provided by the HYPRE library which we access through the PETSc library.

Three important physical parameters for the blood flow are simulated and analyzed: (i) the effect of capillary diameter, (ii) the effect of red cell membrane thickness and (iii) the effect of red cell spacing (hematocrit). The capillary diameter is found out to be particularly important not only for the pressure gradient but also for the deformation of red blood cells. The numerical calculations also indicate a complex shape deformation in which biconcave discoid shape changes to a parachute-like shape which is in accord with the early results in the literature. Furthermore, the parachute-like cell shape in small capillaries undergoes a cupcake shaped buckling instability, which has not been observed in the literature. The instability forms thin rib-like features and the red cell deformation is not axisymmetric but three-dimensional.



KIRMIZI KAN HÜCRELERİ İÇİN ÜÇ BOYUTLU AKIŞKAN YAPI ETKİLEŞİMİ SİMÜLASYONU

ÖZET

Kan reolojisi, kanın akış özelliklerini ve kan içindeki elemanların deformasyon davranışlarını ele alır. Kanın reolojik özellikleri, dokuların beslenmesinde ve atıkların bu dokulardan uzaklaştırılmasında hayati rol oynamaktadır. Çünkü kan, besin maddeleri ve oksijen gibi gerekli maddeleri hücreye taşıırken karbon dioksit, amonyak gibi metabolik atıkları hücreden uzaklaştırır. Buna ek olarak, kanın reolojik özellikleri bağışıklık sisteminde ve vücut sıcaklığının sabit tutulmasında büyük etkilere sahiptir. Kan esas olarak plazma (çoğunlukla suda çözülmüş çeşitli proteinler, glikoz, pıhtılaşma faktörleri, elektrolitler, hormonlar, atık ürünler, vb.), kırmızı kan hücreleri (RBCs), beyaz kan hücreleri (WBCs) ve trombositlerden oluşur. Bu çalışma esas olarak, kırmızı kan hücreleri üzerine yapılmıştır.

Kırmızı kan hücreleri, biyolojik zarla çevrilmiş, neredeyse sıkıştırılmaz olmakla birlikte kesme ve bükülme deformasyonlarına karşı viskoelastik tepki veren, deforme olabilen, çekirdeksiz, sıvı dolu bir kapsül olarak düşünülebilir. Yetişkin sağlıklı bir insan vücudunda, kırmızı kan hücreleri genellikle $8\mu m$ çaplı ve $2\mu m$ kalınlıklı esnek her iki yüzü içbükey diskler halinde şekil almaktadır. Kırmızı kan hücresinin zar yapısı bir çok katmanın bir araya gelmesiyle oluşur. Kalınlığı yaklaşık $5nm$ olan dış lipit çift katmanının elastisitesi, zarın sertliğini etkileyen en önemli faktördür [6]. Kırmızı hücre zar yapısı, dış strese maruz kaldığında kendi çapının yarısı veya daha küçük çapa sahip kılcal damarlardan geçmesine imkan tanıyabilecek kadar büyük deformasyonları kaldırabilecek kabiliyete sahiptir. Normal kırmızı kan hücresinin yüzey alanının hacime oranı, aynı hacimdeki bir küreye göre %40 oranında daha yüksektir [7]. Kırmızı kan hücrelerinin difüzyon yüzeyinin artması sayesinde, dokuların beslenmesinde ve atıkların bu dokulardan uzaklaştırılmasındaki hayati rolünde küreden daha verimli olmasını sağlar. Kan içindeki asılı kırmızı kan hücrelerinin hacim fraksiyonu olarak tanımlanan hematokrit, normal insan kanında %40 ila %45 arasında değişir. Bu oran cinsiyet, yaş ve spor yapma alışkanlıklarına bağlı olarak değişim göstermektedir.

Diğer bütün kan elemanlarının yanı sıra kırmızı kan hücrelerin mekanik özellikleri, kanın reolojik davranışını büyük ölçüde etkiler ve Newtonyen olmayan etkileri beraberinde getirir. Öte yandan, beyaz kan hücreleri kanda hacimce sadece yaklaşık 1/600 oranında bulunurlar ve içindeki akışkanın viskozitesi, kanın viskozitesinden binlerce kez daha büyüktür. Bunun sonucu olarak, aynı akış altındaki kırmızı kan hücreleri kadar deforme olamazlar [8].

Hipertansiyon, sıtma, orak hücre anemisi/hastalığı ve şeker hastalığı gibi bir takım hastalıklar, kırmızı kan hücrelerinin mekanik özelliklerinde değişiklikler oluşturur ve deforme edilebilirliğinin azalmasına neden olur. Kırmızı kan hücrelerinin deformabilitesindeki azalma, mikrovasküler akış direncinde belirgin bir artışa ve

hücrel oksijen alış verişinde ve doku beslenmesinde ciddi derecede azalmaya, mikrosirkülasyonda da bozulmaya neden olur. Bu nedenle, kılcal damardaki kırmızı kan hücrelerini ve onu çevreleyen plazmanın hareket ve deformasyonunu anlamak ilgili hastalıklarla mücadelede değerli bilgiler sağlayabilir.

Büyük damarlardaki kan genellikle sıkıştırılmaz, homojen ve Newtonyen olduğu düşünülür, çünkü kırmızı kan hücrelerinin akış esnasında ne kümelenme ne de deformasyona yetecek kadar zamana sahip olmadığı varsayılmaktadır. Öte yandan, kılcal damar içindeki kan akışı, viskozitesi hematokrit ve kayma oranıyla değişen, homojen ve Newtonyen olmayan bir sıvı olarak modellenmektedir.

Çeşitli akış durumlarındaki kırmızı kan hücresi davranışlarını belirlemek için teorik, deneysel ve sayısal çalışmalar, uzun süredir ilgi gören, aktif bir araştırma alanıdır. Secomb [9], yağlama teorisine dayanan dar kılcal damarlarda kırmızı hücre hareketi için teorik bir model önermiştir ve deneysel verilerle iyi bir uyum içinde olan dar tüplerdeki görünür viskozite değerlerini tahmin etmiştir. Eggleton ve Popel [7] ve Peskin [10] tarafından önerilen daldırılmış sınır yöntemini (immersed boundary method) damar içi akışa adapte ederek, RBC'ler için zar-sıvı akış etkileşimlerinin üç boyutlu simülasyonlar sunmuştur. Liu et al. [11], daldırılmış sonlu elemanlar yöntemini (IFEM) protein moleküllerinin dinamikleriyle birleştirerek kan hücrelerinin kümelenmesini ve bu davranışın kan reolojisi üzerindeki etkilerini araştırmıştır. Hücre zarının hem kesme hem de bükülme sertliğini hesaba katabilmek için, kırmızı kan hücresi üç boyutlu katı elemanlarla modellenmiştir. Daha sonraki bir çalışma da, Liu and Liu [12], üç boyutlu olarak, mikro ve kılcal damarlar içinde bulunan RBC'lerde meydana gelen büyük deformasyonu incelemek için, daldırılmış (immersed) sonlu elemanlar yöntemini çözüm ağsız (meshfree) yöntemlerle birleştirip doğrusal olmayan katı maddeler için uygulamışlardır. Yazarlar, RBC rouleau'nun farklı kesme oranlarında ayrıştırılmasını incelemeye çalışmışlardır.

Sonlu zar kalınlığına sahip kırmızı kan hücrelerinde akış yapı etkileşimiyle ilgili sınırlı sayıda çalışma mevcuttur. Oysa ki, akışkan yapı etkileşimi (FSI) literatürdeki çoklu fizik problemleri içinden sıklıkla başvurulan modelleme tekniklerinden birisidir. FSI, akışkan ile bu akışkanın çevrelediği veya içerisinde bulunduğu katı yapıyla olan etkileşimi konu alır. Kırmızı kan hücreleri de FSI'nın inceleme konuları arasında yer alabilir. Çünkü kan hücresinin zarı dışarıdan kan plazması ve içeriden hemoglobin olmak üzere iki akışkan yapıyla etkileşim içindedir.

Bu çalışmada, problemin akışkan bölgesi için daimi olmayan; sıkıştırılmaz Navier-Stokes denklemi, Keyfi Lagrangian-Eulerian (ALE) formülasyonuna dayanan, kenar merkezli (side-centered) yapısal olmayan sonlu hacimler yöntemiyle ayrıklaştırılmıştır. Yapısal alanıysa, Lagrangian çerçevesinde Saint Venant-Kirchhoff malzeme modeli için klasik Galerkin sonlu element yöntemi ile ayrıklaştırılmaktadır. Klasik bölünmüş (partitioned) yaklaşımlar, Dirichlet sınır koşuluyla çevrelenmiş akışkanın FSI iterasyonları sırasında akışkanın sıkıştırılmazlığını sağlayamamaktadır. Bahsi geçen bu problem kan hücresinin sınır koşullarını çevreleyen sistemlerde de görülmür. Bu nedenle, tam bağlaşıklık akışkan-yapı etkileşim algoritması gerekmektedir. Mevcut çalışmada, akışkan ve yapı alanının çözümü tam bağlaşıklık bir yaklaşıma dayanmaktadır. Bu sayede kılcal damar içerisindeki kırmızı kan hücresinin deformasyonunun sayısal simülasyonu için, akışkan ve yapı denklemleri tek bir denklem sistemi olacak şekilde şekillendirilip, çözüm her adımda tam bağlaşıklık olarak elde edilmektedir. Mevcut yaklaşım aynı zamanda global ayrık geometrik karunum yasası

(global discrete geometric conservation law (DGCL)) sağlamak için katı ve akışkan alanlar arasındaki ara yüzeyde uyumlu bir kinematik sınır koşulu sağlar. Bu sayede, kırmızı kan hücresi içindeki sıvı (hemoglobin) kütlesi simülasyon boyunca makine hassasiyetinde korunur.

Çalışma kapsamında kan akışı için üç önemli fiziksel parametre simüle ve analiz edilecektir: (i) kılcal damar çapının etkisi, (ii) kırmızı hücre zar kalınlığının etkisi ve (iii) kırmızı hücre aralığının (hematokrit) etkisi. Kılcal damar çapının, sadece basınç gradyanı için değil, aynı zamanda kırmızı kan hücrelerinin deformasyonu için özellikle önemli olduğu bulunmuştur. Sayısal hesaplamalar, biconcave diskoid şeklinin, literatürdeki sonuçlara uygun olarak paraşüt benzeri bir şekle dönüştüğünü de göstermiştir. Buna ek olarak, küçük kılcal damarlardaki paraşüt benzeri hücre şekli, literatürde gözlemlenmemiş bir cupcake şekillinde bükülme (buckling) kararsızlığına maruz kaldığı gözlemlenmektedir. Kararsızlık, kırmızı kan hücresi etrafında düşük dalga boylu deformasyonlar oluşturur ve kırmızı hücre deformasyonu, aksisimetrik değil, üç boyutludur.

Bu tezin geri kalanı şu sırayla düzenlenmiştir: Bölüm 1, motivasyon ve detaylı literatür taramasını kapsamaktadır. Bölüm 2, mevcut FSI algoritmasının yeni ve tam bağlaşıklık (monolitik) iteratif yöntemi ile birlikte kısa bir açıklama sunmaktadır. Bölüm 3'te, kırmızı kan hücresinin geometrisi ve fiziksel parametreleri verilmiştir. Ayrıca, problemin sınır koşulları bu bölümde verilmektedir. Bölüm 4 ve 5'de sırasıyla iki ve üç boyutlu analiz sonuçları yer almaktadır. Mevcut çalışmanın çıkarımlarına bölüm 6'da değinilmiştir.



1. INTRODUCTION

1.1 Purpose of Thesis

Hemorheology, also called as blood rheology, deals with the flow properties of blood as well as the deformation behavior of its formed elements. The rheological properties of blood play a vital role for appropriate tissue perfusion, since blood delivers necessary substances such as nutrients and oxygen to the cells and transports metabolic waste products such as carbon dioxide, ammonia, etc. away from those same cells. In addition, these rheological properties have major effects on the immune system. The blood mainly contains plasma, which is composed of mostly water with a variety of dissolved proteins, glucose, clotting factors, electrolytes, hormones, waste products, etc., and living cells, which are red blood cells (RBCs) (or erythrocytes), white blood cells (WBCs) (or leukocytes), and platelets (or thrombocytes) as illustrated in Figure 1.1.

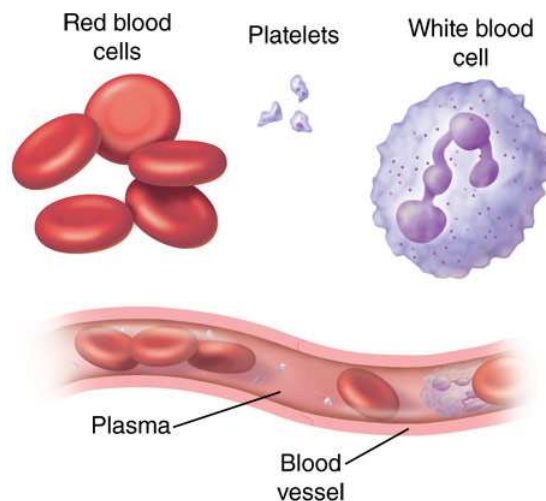


Figure 1.1 : Illustration of red blood cells (RBCs) (or erythrocytes), white blood cells (WBCs) (or leukocytes), and platelets (or thrombocytes).

The red blood cells can be considered as a deformable, nucleus-free fluid-filled capsule enclosed by a biological membrane, that is nearly incompressible and exhibits a viscoelastic response to shearing and bending deformation. A mature human red blood

cell normally takes the form of flexible biconcave disc, which is approximately about $8\mu\text{m}$ in diameter and $2\mu\text{m}$ in thickness. The red cell membrane is composed of several layers and the stiffness of the membrane is mainly dominated by the elasticity of the outer lipid bilayer, which has approximately 5nm thickness [6]. The red cell membrane structures have the ability to undergo remarkably large deformations when subjected to external stresses, which allow them to pass through capillaries with half the diameter of the RBC or less. The surface area to volume ratio of the normal RBC cell is 40% greater than that of a sphere with the same volume [7]. The hematocrit, which is defined as the volume fraction of the suspended red blood cells inside blood, varies between 40 to 45% for normal human blood. Therefore, the mechanical properties of red cells strongly influence the rheological behavior of blood and introduce non-Newtonian effects. Apparent viscosity of blood as a function of shear rates and hematocrit effects on blood as a function of shear rates are given in Figure 1.2 [1]. On the other hand, the white blood cells occupy only about 1/600th of blood by volume and have an internal viscosity thousands times larger than the viscosity of blood, and thus do not deform as much as the red blood cells under the same flow conditions [8].

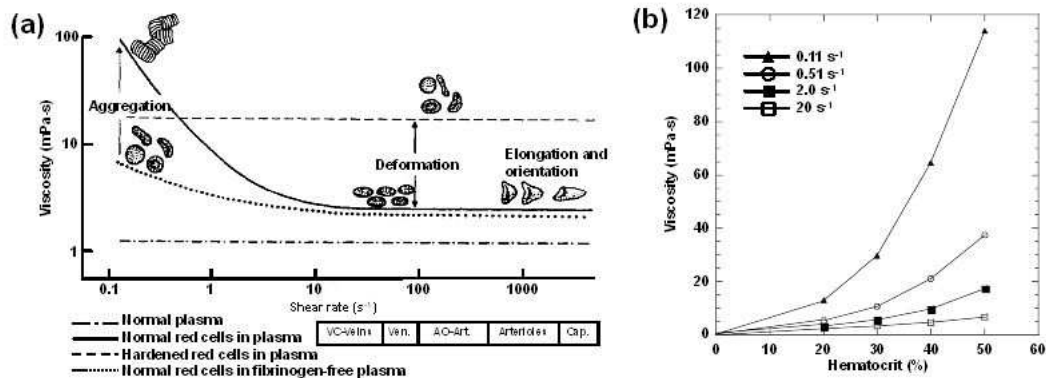


Figure 1.2 : Apparent viscosity of blood as a function of shear rates [a] and hematocrit effects on blood as a function of shear rates [b].

In a number of human diseases such as hypertension, malaria, sickle cell anemia/disease and diabetes mellitus, variations in the mechanical properties of red blood cells occur and cause reduced deformability. A decrease in red cell deformability causes a significant increase in microvascular flow resistance and a decrease in cellular oxygen delivery and tissue oxygenation, an impairment of microcirculation. Therefore, it is of great importance to understand the motion and deformation of the RBCs and

the surrounding plasma in capillaries, which may provide valuable knowledge in the fight against the relevant diseases.

1.2 Literature Review

Theoretical, experimental and numerical studies to determine the red cell behaviors in various flow situations have been a longstanding and active area of research. Figure 1.3 [2] shows that human red blood cells whose flow directions are from left to right, flowing in glass tubes with approximate diameters of $4.5\mu m$ (top), $7\mu m$ (center) and $15\mu m$ (bottom), respectively. Secomb [9] proposed a theoretical model for red cell motion in narrow capillaries based on lubrication theory and predicted the values of apparent viscosity in narrow tubes, which are in good agreement with experimental data. Pozrikidis [13] employed the boundary integral method for the axisymmetric motion of a periodic array of red cells with arbitrary cell separations and tube diameters in the context of the Stokes flow and the nearly incompressible and elastic behavior of the cell membrane with respect to shearing and bending deformation is taken into consideration. Eggleton and Popel [7] adapted the immersed boundary method proposed by Peskin [10] and presented the three-dimensional simulations of membrane-fluid flow interactions for RBCs. Liu et al. [11] coupled the immersed finite element method (IFEM) with protein molecular dynamics to investigate the behaviors of RBC aggregates and their effects on the blood rheology. To account for both membrane shear and bending stiffness, RBC membrane is modelled with three-dimensional solid elements. In a later study, Liu and Liu [12] combined the

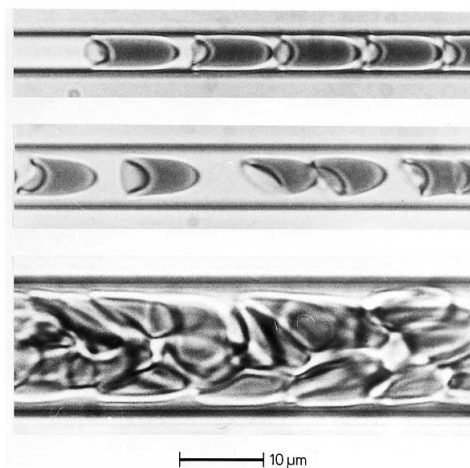


Figure 1.3 : Human red blood cells flowing in glass tubes.

immersed finite element method with meshfree methods for nonlinear solids to handle the large deformation of RBCs within micro and capillary vessels in three-dimensions. The authors attempted to study the disaggregation of an RBC rouleau at different shear rates. Zhang et al. [14] developed a lattice Boltzmann algorithm to simulate the RBC behavior in shear and channel flows. The immersed boundary method is employed to incorporate the fluid-membrane interactions. The phenomena of microscopic blood flows, such as cell-free layers, blunt velocity profiles, and the Fåhræus effect [15] have also been reproduced. In another study, Zhang et al. [16] considered the RBC membrane mechanics, plasma/cytoplasm viscosity difference, intercellular interaction, and the hydrodynamic viscous forces in their two-dimensional numerical simulations. Le et al. [17] developed an implicit immersed boundary method for the incompressible Navier-Stokes equations capable of handling three-dimensional membrane-fluid flow interactions and applied the numerical algorithm to simulate the large deformation of human RBCs subjected to direct stretching by optical tweezers. Hosseini and Feng [18] presented a two-dimensional particle-based model for the red blood cells and the cell membrane is replaced by a set of discrete particles connected by nonlinear springs. The cytoplasm and the external liquid are discretized by particles as in standard smoothed particle hydrodynamics (SPH) solution of the Navier-Stokes equations. The numerical approach were extended to three-dimensions in Hosseini and Feng [19] and applied to the steady-state cell stretching of a healthy or malaria-infected RBCs by optical tweezers. Zhao et al. [4] presented a spectral element based boundary integral method for the Stokes flow and investigated the interactions of large numbers of blood cells as encountered in blood flows in the microcirculation. Wang and Xing [20] studied the dynamics of the axisymmetric, pressure driven motion of RBCs in capillaries using the immersed boundary method and recreated several important in vivo hemodynamic and hemorheological properties of microscopic blood flow, such as parachute shape of the cells, blunt velocity profile, and the Fåhræus effect. Ye et al. [21] presented a particle level set method in conjunction with a modified SIMPLER algorithm on a fixed staggered Cartesian mesh in order to investigate the effects of RBC diameter, elastic modulus, bending stiffness of RBC membrane, initial flow velocity as well as plasma/cytoplasm density and viscosity ratios. In a later work, Ye et al. [22] developed a three-dimensional computational model using the dissipative particle dynamics (DPD) method in conjunction with a Morse potential to account

cell-cell interactions. Huang et al. [23] proposed an improved penalty immersed boundary method (pIBM) for the simulation of the flow-induced deformation of three-dimensional elastic capsules, including biconcave capsule as a model of RBC, and the numerical simulations indicated the formation of buckling in a linear shear flow. Reasor Jr et al. [24] implemented a spectrin-link (SL) red blood cell membrane method coupled with a lattice Boltzmann method to construct a computationally efficient numerical algorithm for the simulation of realistic suspensions of RBCs. Freund [25] employed boundary integral model to simulate the passage of a blood cell through a particularly narrow geometry motivated by the human spleen and observed several distinct behaviors based on flow rates and cytosol viscosities. Shi et al. [5] combined the numerical technique derived from the lattice Boltzmann method and the distributed Lagrange multiplier/fictitious domain method with a mesoscopic membrane model in order to study hydrodynamic interactions between RBCs. Chivuka et al. [26] simulated deformation of a biconcave red blood cell in a fully developed Poiseuille flow through a capillary using the NURBS-based isogeometric analysis combined with the immersed boundary method proposed by Peskin [10]. Hashemi and Rahnama [27] proposed a three-dimensional hybrid method, combining lattice Boltzmann method for plasma flow, finite element method for RBC membrane analysis, and immersed boundary method for their interaction. The effect of membrane deformability, its initial orientation, velocity, and flow pressure gradient are investigated. More recently, Balogh and Bagchi [28] have presented a large-scale computational methodology based on the immersed boundary methods for modeling cellular-scale blood flow in complex geometries. We refer to the review articles by Freund [29] and Jua et al. [30] on the further details of the numerical algorithms.

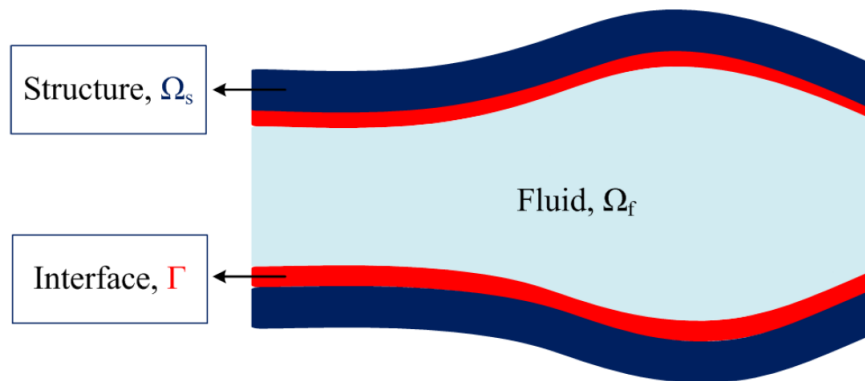


Figure 1.4 : Mathematical FSI domain.

In contrast to the above studies, there are very limited works on the fluid-structure interaction (FSI) of red blood cells based on body conformal meshes with a finite membrane thickness. The FSI problem can be basically defined as the interaction between surrounding fluid and deformable solid structure, as seen in Figure 1.4 [3]. The main working areas of FSI is aeroelastic phenomena which contain as flutter, buffeting and divergence, design of offshore structures, structural effect of strong wind on bridges and tall buildings, flow induced vibrations in heat exchangers tubes, explosions or high-velocity impacts, large class of acoustic problems. FSI is also a preferred aspect for biomechanic which include blood flow in vessel, deformation of blood cell or animal locomotion. As mentioned before, the use of FSI algorithm for the deformation of red blood cells is limited. To the best of our knowledge, only Klöppel and Wall [31] employed the fluid-structure interaction algorithm with finite thickness solid shell elements in three-dimensions for the red cell membrane and investigated the mechanical behavior of human red blood cell filled with a Newtonian fluid in optical tweezers. The main reason is that the classical partitioned (segregated) approaches can not satisfy the incompressibility constraint of the fluid during standard alternating FSI iterations when the fluid domain is entirely enclosed by all Dirichlet boundary conditions as pointed out by Küttler et al. [32]. This is also the case for the incompressible cytoplasmic fluid within the solid red cell membrane since the incompressible fluid boundary condition for the cytoplasmic fluid is not necessarily compatible during alternating FSI iterations ($\oint_{\Gamma} \mathbf{n} \cdot \mathbf{u} dS \neq 0$) and the segregated divergence-free fluid solver will fail to converge. In addition, the explicit partitioned methods generally employs fixed point (Picard type) iterations and the standard fixed point iterations may diverge in the presence of strong fluid-structure coupling due to the high fluid/structure density ratio, similar to that of the cytoplasmic fluid to RBC membrane, which causes the so-called artificial added mass effect [33]. Therefore, a fully coupled (monolithic) FSI algorithm has to be employed for these balloon-type problems. There is also problem with high aspect ratio of the three-dimensional solid shell elements employed within relatively thin lipid bilayer ($5nm$), which leads to a very bad condition number [34]. The high aspect ratio computational domains such as long capillaries also adversely affect the convergence of iterative method. These numerical difficulties poses significant challenges for the FSI algorithms based on body conformal meshes with a finite membrane thickness. In the current paper, we

employ the monolithic FSI algorithm proposed in Eken and Sahin [35, 36] with a new preconditioner in order to simulate the flow-induced deformation and transport of the red blood cells in blood plasma flowing through small capillaries. In the present approach, the fluid domain is discretized using the stable side-centered unstructured finite volume method based on Arbitrary Lagrangian-Eulerian (ALE) formulation, meanwhile the solid domain is discretized with the classical Galerkin finite element formulation for the Saint Venant-Kirchhoff material in a Lagrangian frame. The method employs conformal hexahedral elements at the fluid-solid interface in order to accurately resolve sharp gradients. In addition, the local and global geometric conservation laws (DGCL) [37] are satisfied at discrete level and the compatible kinematic boundary condition is applied at the fluid-solid interface [36], which leads to the conservation of cytoplasmic fluid mass at machine precision. In the current paper, the resulting large-scale algebraic linear systems are solved in a fully coupled (monolithic) manner using the FGMRES(m) Krylov iterative method [38] preconditioned with a matrix factorization similar to that of the projection method [39] for the whole system and the parallel algebraic multigrid solver BoomerAMG is used for the scaled discrete Laplacian provided by the HYPRE library [40] which we access through the PETSc library [41]. The present new block preconditioner may be considered as the extension of the classical projection method [39] to FSI problems.

In order to better understand the phenomenon associated with the blood flow in small capillaries, the above monolithic FSI algorithm has been employed to investigate the transport and deformation of red cells in small capillaries, with the main focus on gaining a greater insight into the influences of those cells to the plasma flow. As far as our knowledge, the three-dimensional mechanical behaviors of red blood cells in capillaries have not been investigated using a FSI algorithm based on body conformal meshes with a finite membrane thickness. In the literature, the simulations of RBCs indicate that the bending stiffness must be included [7] in order to simulate more complex red cell deformations, since it plays an important role in the mechanical behavior of RBCs, especially at the locations with sharp changes in curvature [21]. The present FSI approach with a finite membrane thickness naturally leads to the bending rigidity and it does not require complex local curvature calculations (e.g., [42]). In order to better analyse the blood flow in small capillaries, the numerical simulations

conducted in this paper include parametric studies on the effects of capillary diameter, red cell membrane thickness, and red cell spacing (hematocrit). The calculations indicate that the biconcave discoid shape in large capillaries changes to a parachute-like shape, which is in accord with the early experimental and numerical results in the literature. However, the numerical simulations for small capillaries illustrate that the parachute-like cell shape undergoes a cupcake shaped buckling instability due to the compressive elastic tension forces along the membrane surface, which has not been noted in the literature. The buckling instability forms thin rib-like features and the membrane deformation is no longer axisymmetric but three-dimensional. In the literature, the buckling behavior of red cells has been observed only in the case of a red cell passing through a very narrow neck [4] and a red cell in a simple shear flow [23] as well as at cell-cell interface for the aggregation of red blood cells [43] and the present cupcake shaped buckled red cell geometry is completely new. The similar buckling instability is also observed for a spherical fluid-filled capsule as it passes through a circular tube with a diameter less than that of the capsule [44]. However, the spherical capsules in a circular tube with the blockage ratios and capillary numbers close to the present values do not indicate any rib-like features and only the trailing end buckles inward [45]. The spherical capsules in a simple shear also indicates buckling behavior [23, 46–49], where the spherical capsule initially deforms into a nearly ellipsoidal shape with an inclination angle and then buckles around the equator. However, the buckling on the red cell membrane is relatively more complex due to its initial biconcave discoid shape compared to that of the oblate spheroidal capsule. As pointed out by Huang et al. [23], the buckling of a spherical fluid-filled capsule in a simple shear indicate that the buckling on the surface of a biconcave capsule leads more wrinkles and complex deformations as compared to those of the oblate spheroidal case. In addition, the buckling instability in a simple shear is observed to occurs near the equator of the capsule for small shear rates but near the tips for large shear rates.

1.3 Outline

The remainder of this thesis is organized as follow: chapter 2 provides a brief description of the present FSI algorithm along with the new fully coupled (monolithic) iterative method. Geometry and physical parameter of red blood cell is described in

chapter 3. In addition, the physical boundary conditions are given in this section. In chapter 4 and 5, the FSI algorithm has been initially validated by performing spatial and temporal converge studies for a single cell in a narrow capillary and then employed to analyse (i) the effect of capillary diameter, (ii) the effect of red cell membrane thickness, and (iii) the effect of the red cell spacing (hematocrit) in two- and three-dimensions. The three-dimensional cupcake shaped buckling instability in small capillaries is discussed in detail. The final conclusions of the present work are provided in chapter 6.





2. GOVERNING EQUATIONS

2.1 Fluid Equations

The integral form of the incompressible Navier-Stokes equations for an arbitrary moving control volume $\Omega(t)$ with boundary $\partial\Omega(t)$ can be written in the Cartesian coordinate system in dimensional form as follows: the momentum equation

$$\rho_f \frac{\partial}{\partial t} \int_{\Omega} \mathbf{u} dV + \rho_f \oint_{\partial\Omega} [\mathbf{n} \cdot (\mathbf{u} - \dot{\mathbf{x}})] \mathbf{u} dS = \oint_{\partial\Omega} \boldsymbol{\sigma}_f \mathbf{n} dS \quad (2.1)$$

the continuity equation

$$- \oint_{\partial\Omega} \mathbf{n} \cdot \mathbf{u} dS = 0 \quad (2.2)$$

In here, V is the control volume, S is the control volume surface area, \mathbf{n} is the outward normal vector, ρ_f is the constant fluid density, \mathbf{u} is the local fluid velocity vector, $\dot{\mathbf{x}}$ is the grid velocity, and $\boldsymbol{\sigma}_f$ is the fluid stress tensor. The constitutive relation for an incompressible Newtonian fluid is given by

$$\boldsymbol{\sigma}_f = -p\mathbf{I} + \mu_f(\nabla\mathbf{u} + \nabla\mathbf{u}^\top) \quad (2.3)$$

where p is the fluid pressure and μ_f is the fluid dynamic viscosity.

2.2 Solid Equations

The balance of the linear momentum equation in the Lagrangian framework, where the material derivative becomes a partial derivative with respect to time, can be written as

$$\rho_s \frac{\partial^2 \mathbf{d}}{\partial t^2} = \nabla \boldsymbol{\sigma}_s \quad (2.4)$$

where ρ_s is the spatial density, \mathbf{d} is the displacement vector, and $\boldsymbol{\sigma}_s$ is the Cauchy stress tensor defined using the following constitutive law for the Saint Venant-Kirchhoff material

$$\mathbf{S} = J\mathbf{F}^{-1}\boldsymbol{\sigma}_s\mathbf{F}^{-\top} \quad (2.5)$$

$$\mathbf{F} = (\mathbf{I} + \nabla\mathbf{d}) \quad (2.6)$$

$$E = \frac{1}{2}(\mathbf{F}^\top \mathbf{F} - \mathbf{I}) \quad (2.7)$$

$$\mathbf{S} = \lambda_s \text{trace}(\mathbf{E})\mathbf{I} + 2\mu_s \mathbf{E} \quad (2.8)$$

$$\mathbf{\Pi} = \mathbf{F}\mathbf{S} \quad (2.9)$$

where \mathbf{S} is the second Piola-Kirchhoff stress tensor, \mathbf{F} is the deformation gradient tensor, $J = \det(\mathbf{F})$ is the deformation gradient determinant, \mathbf{E} is the Green-Lagrange strain tensor, $\mathbf{\Pi}$ is the non-symmetric first Piola-Kirchhoff stress tensor, and λ_s and μ_s are the material Lamé's constants. These Lamé's values can be computed from the material Young's modulus E and the Poisson ratio ν as $\lambda_s = E\nu/(1+\nu)(1-2\nu)$ and $\mu_s = E/2(1+\nu)$. Then, the equation of motion with respect to the initial configuration is given by

$$\rho_0 \frac{\partial^2 \mathbf{d}}{\partial t^2} = \nabla_0 \cdot \mathbf{\Pi}^\top \quad (2.10)$$

where ρ_0 is the solid material density per unit undeformed volume and ∇_0 indicates the gradient with respect to the reference (undeformed) configuration.

2.3 Interface Conditions

Interface conditions require two main conditions across the fluid-structure interface at all times. These are the kinematic and the dynamic continuity conditions. The kinematic boundary condition on the common fluid-structure interface is driven by continuity of the velocity.

$$\mathbf{u} = \dot{\mathbf{d}} \quad (2.11)$$

The dynamic condition holds for surface traction vector at the common fluid-structure interface.

$$\boldsymbol{\sigma}_s \mathbf{n}_s = -\boldsymbol{\sigma}_f \mathbf{n}_f \quad (2.12)$$

where $\boldsymbol{\sigma}_s$ is the Cauchy stress tensor of the solid domain and $\boldsymbol{\sigma}_f$ is the fluid stress tensor in the case of an incompressible Newtonian fluid.

2.4 Fully Coupled Solver

The spatial and temporal discretization of the governing equations along with the interface conditions are provided in Eken and Sahin [35, 36] in detail. In the present FSI algorithm, the fluid domain is discretized using the side-centered unstructured

finite volume method based on Arbitrary Lagrangian-Eulerian (ALE) formulation [50], meanwhile the solid domain is discretized with the classical Galerkin finite element formulation for the Saint Venant-Kirchhoff material in a Lagrangian frame. The time integration method for the solid domain is based on the Newmark type generalized- α method while the second-order backward difference (BDF2) is used in the fluid domain. The compatible kinematic boundary condition [36] is applied at the interface between the solid and fluid domains in order to satisfy the global discrete geometric conservation law (DGCL) [37], which leads to the mass conservation of the cytoplasmic fluid within the red cell at machine precision. The resulting system of nonlinear algebraic equations can be given in the following block structure form including the velocity, displacement and pressure unknowns:

$$\begin{bmatrix} A_{uu} & A_{ud} & A_{up} \\ A_{du} & A_{dd} & A_{dp} \\ A_{pu} & 0 & 0 \end{bmatrix} \begin{bmatrix} \mathbf{u}^{n+1} \\ \Delta \mathbf{d}^{n+1} \\ p^{n+1} \end{bmatrix} = \begin{bmatrix} d_1 \\ d_2 \\ 0 \end{bmatrix} \quad (2.13)$$

In here, the first row of blocks corresponds to the fluid momentum equations and the kinematic boundary conditions. The first column is due to the fluid convection-diffusion and time derivation parts, the second column is due to the ALE mesh motion and the last column is due to the pressure gradient. The second row represents the fluid mesh deformation equations, the solid momentum equations and the FSI dynamic boundary conditions. The last row is due to the fluid mass conservation. However, it is rather difficult to construct robust preconditioners due to the presence of the zero-block diagonal resulting from the divergence-free constraint. For the first preconditioner, an upper triangular right preconditioner matrix, which results in a scaled discrete Laplacian instead of a zero block in the original system, is used. Then, the modified system becomes:

$$\begin{bmatrix} A_{uu} & A_{ud} & A_{up} \\ A_{du} & A_{dd} & A_{dp} \\ A_{pu} & 0 & 0 \end{bmatrix} \begin{bmatrix} I & 0 & A_{up} \\ 0 & \Delta t & 0 \\ 0 & 0 & I \end{bmatrix} \begin{bmatrix} \mathbf{q}^{n+1} \\ \mathbf{r}^{n+1} \\ p^{n+1} \end{bmatrix} = \begin{bmatrix} A_{uu} & \Delta t A_{ud} & A_{uu} A_{up} + A_{up} \\ A_{du} & \Delta t A_{dd} & A_{du} A_{up} + A_{dp} \\ A_{pu} & 0 & A_{pu} A_{up} \end{bmatrix} \begin{bmatrix} \mathbf{q}^{n+1} \\ \mathbf{r}^{n+1} \\ p^{n+1} \end{bmatrix} = \begin{bmatrix} d_1 \\ d_2 \\ 0 \end{bmatrix} \quad (2.14)$$

where $\mathbf{q}^{n+1} = \mathbf{u}^{n+1} - A_{up} p^{n+1}$ and $\mathbf{r}^{n+1} = \Delta \mathbf{d}^{n+1} / \Delta t$. The second term \mathbf{r}^{n+1} corresponds to the nodal velocity vector for the mesh motion and it is comparable (same order) with the fluid velocity. The multiplication with Δt helps to reduce

large non-zero entries in the off-diagonal block A_{ud} due to the $1/\Delta t$ term resulting from the mesh motion for a better preconditioning. Then, a one-level restricted additive Schwarz preconditioner with a block-incomplete factorization within each partitioned sub-domain is utilized. The implementation of the preconditioned Krylov subspace algorithm, matrix-matrix multiplication, and the restricted additive Schwarz preconditioner are carried out using the PETSc [41] software package developed at the Argonne National Laboratories. The second preconditioner is based on a block factorization. In the literature, the block parallel preconditioners for the coupled linearized FSI system have been extensively studied. Heil [51] proposed a block factorization based on neglecting the fluid-solid or solid-fluid interaction blocks. Deparis et al. [52] used a similar preconditioner based on dropping the block associated with the transpose of the kinematic coupling condition. In these approaches, the two-way coupling between the fluid and solid domains is ignored at the preconditioning level. This is improved in the block preconditioner proposed by Langer and Yang [53] based on the complete LDU factorization of the coupled system matrix, where L, D and U matrices are approximated using the sub-block matrices. The present approach is motivated by the relatively simple LDU factorization of the projection method [39] assuming that the time step is small and the viscous (not pressure) forces can be neglected. Then, the preconditioner matrix P_1 can be approximated as

$$P_1 = \begin{bmatrix} I & A_{ud} & A_{up} \\ 0 & I & A_{dp} \\ A_{pu} & 0 & 0 \end{bmatrix} = \begin{bmatrix} I & 0 & 0 \\ 0 & I & 0 \\ A_{pu} & -A_{pu}A_{ud} & I \end{bmatrix} \begin{bmatrix} I & 0 & 0 \\ 0 & I & 0 \\ 0 & 0 & S_{pp} \end{bmatrix} \begin{bmatrix} I & A_{ud} & A_{up} \\ 0 & I & A_{dp} \\ 0 & 0 & I \end{bmatrix} \quad (2.15)$$

where $S_{pp} = -A_{pu}A_{up} + A_{pu}A_{ud}A_{dp}$. The exact inverse of the first and third matrices can be easily computed since the matrices are triangular. Then P_1^{-1} can be computed as

$$P_1^{-1} = \begin{bmatrix} I & -A_{ud} & A_{ud}A_{dp} - A_{up} \\ 0 & I & -A_{dp} \\ 0 & 0 & I \end{bmatrix} \begin{bmatrix} I & 0 & 0 \\ 0 & I & 0 \\ 0 & 0 & S_{pp}^{-1} \end{bmatrix} \begin{bmatrix} I & 0 & 0 \\ 0 & I & 0 \\ -A_{pu} & A_{pu}A_{ud} & 1 \end{bmatrix} \quad (2.16)$$

For the second matrix, the matrix inverse S_{pp}^{-1} is approximated by employing two steps of the parallel algebraic multigrid solver BoomerAMG provided by the HYPRE library [40], which we access through the PETSc library [41]. The coarsening scheme is set to the Parallel Modified Independent Set (PMIS) algorithm [54] within the BoomerAMG library in order to reduce the complexity. The implementation of the preconditioning operation is carried out by using the PCSHELL option provided

within the PETSc library. Then the right preconditioned system of algebraic equation is solved using the Flexible Generalized Conjugate Residual Method-FGMRES(m) proposed by Saad [38], since it allows the variations within the preconditioner between iterations. In here, $A_{pu}A_{ud}A_{dp}$ term of the S_{pp} matrix should not be neglected, since the eigenvalue analysis of the $A_{pu}A_{up}$ matrix indicates that one of its eigenvalues is zero (the number is actually equal to the number of RBCs) due to the decoupling of the pressure fields between the inner cytoplasmic fluid and the exterior plasma fluid. The present second preconditioner can be further improved by employing the following block factorization.

$$P_2^{-1} = \begin{bmatrix} I & A_{ud} & A_{up} \\ 0 & I & S_{dp} \\ A_{pu} & 0 & 0 \end{bmatrix}^{-1} \begin{bmatrix} I & 0 & 0 \\ 0 & S_{dd} & 0 \\ 0 & 0 & I \end{bmatrix}^{-1} \begin{bmatrix} I & 0 & 0 \\ A_{du} & I & 0 \\ 0 & 0 & I \end{bmatrix}^{-1} = \begin{bmatrix} I & A_{ud} & A_{up} \\ A_{du} & A_{dd} & A_{dp} \\ A_{pu} & 0 & 0 \end{bmatrix}^{-1} \quad (2.17)$$

where $S_{dp} = A_{dd}^{-1}A_{dp}$ and $S_{dd} = A_{dd} - A_{du}A_{ud}$. In here, the S_{dp} term is approximated as $S_{dp} = \text{diag}(A_{dd})^{-1}A_{dp}$, where $\text{diag}(A_{dd})$ represents the diagonal entries of the A_{dd} matrix. The above first matrix is factorized using the same approach in the equation 2.15 and it is approximated by employing one step of the parallel algebraic multigrid solver BoomerAMG. The PCFIELDSPLIT preconditioner within the PETSc library is used for the second matrix to implement the block preconditioner for the S_{dd} matrix corresponding the each components of the displacement vector and the parallel algebraic multigrid solver BoomerAMG is also used for the each diagonal blocks. The eigenspectrum analysis of the S_{dd} indicates that the $-A_{du}A_{ud}$ term should not be neglected since the A_{dd} matrix for the solid equations with zero Dirichlet boundary condition leads to a singular system (six zero eigenvalues in three-dimensions for a single RBC) in the case of a zero solid density due to the rigid body modes corresponding to translations and rotations [55]. Although the solid density is not zero and the mass matrix shifts these zero eigenvalues, their values are still relatively small. The $-A_{du}A_{ud}$ term improves these eigenvalues and the zero solid density can also be used. Therefore, the present block preconditioners are carefully constructed for the blocks corresponding to both the nodal displacement vector and the pressure not to lead to a singular system, which may cause convergence issues. Although the BoomerAMG solver with the near null spaces corresponding to the translational and rotational rigid modes can be directly used for the solid displacement equations [55], it is not as effective as the above block preconditioning. In the current paper, we employ the second preconditioner for the three-dimensional simulations, since the first

preconditioner with ILU(0) and ILU(1) fails to converge for large aspect ratio domains. The calculations also indicate that the convergence rate of the second preconditioner is not significantly affected by the computational domain aspect ratio, such as RBCs in long capillaries. For the both preconditioned iterative methods, the block matrices and the right hand side corresponding to the momentum and displacement equations are scaled using the matrix diagonal entries, meanwhile the absolute row sum value is used for the continuity equation. The computational domain is decomposed into a set of partitions using the METIS library [56].



3. DESCRIPTION OF THE PROBLEM

In this section, geometry and physical parameter of red blood cell is described. In addition, the physical boundary conditions are given in this section.

3.1 Red Blood Cell Geometry

The geometry of the red blood cell is provided in Figure 3.1 and the outer surface of the red blood cell is defined as [57, 58]

$$T(r) = \pm \sqrt{1 - (r/R_0)^2} [C_0 + C_1(r/R_0)^2 + C_2(r/R_0)^4] \quad (3.1)$$

where $T(r)$ is the thickness of RBC in the x -direction as a function of the distance $r = \sqrt{y^2 + z^2}$, and R_0 is the initial radius of RBC. We assume that $R_0 = 3.9\mu m$, $C_0 = 0.81\mu m$, $C_1 = 7.83\mu m$ and $C_2 = -4.39\mu m$. The minimum thickness is $T_1 = 0.81\mu m$ and the maximum thickness is $T_2 = 2.4\mu m$. The diameter of the red blood cell is $D = 7.8\mu m$. The red cell membrane spans approximately 40–50 nm in thickness [59, 60] and the present inner surface of the red blood cell is created with an inward

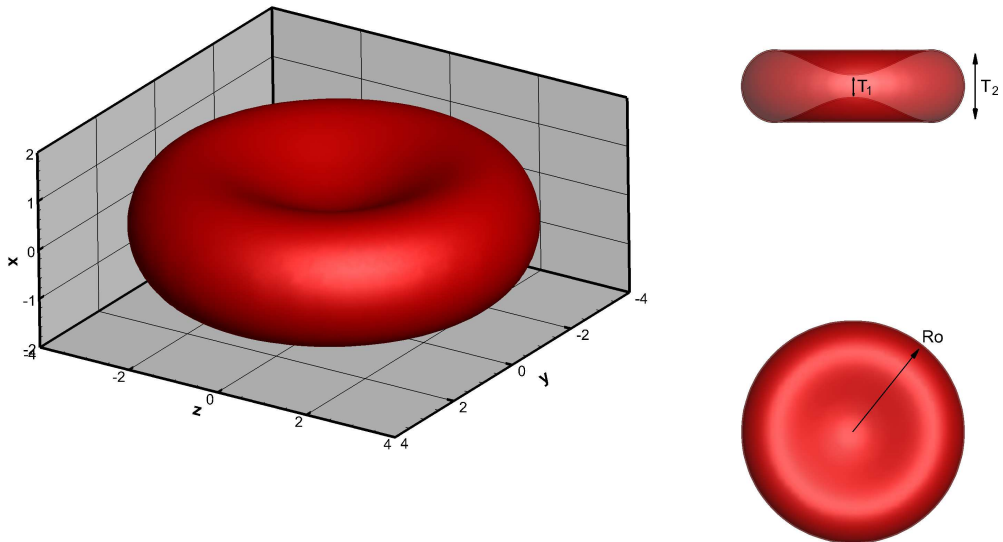


Figure 3.1 : Geometry of red blood cell.

thickness of $h = 0.05\mu m$ ($50nm$). The physical parameters of the red blood cell and fluid plasma are tabulated in Table 3.1. The experimental value of the Young's modulus for the whole membrane is approximately $4.4kPa$ ($4.4pg/\mu s^2\mu m$) for a healthy red blood cell [6]. However, the membrane is composed of several layers and the stiffness of the membrane is mainly dominated by the elasticity of the outer lipid bilayer, which has a $5nm$ thickness [6]. However, numerically it is not possible to reach an adequate mesh resolution to resolve the lipid bilayer due to the bad condition number of solid shell elements with high aspect ratio in three-dimensions [34]. The theory of plates and shells indicates that the flexural/bending rigidity ($Eh^3/12(1 - \nu^2)$) is proportional to the cubic power of the wall thickness, meanwhile the extensional rigidity (Eh) is proportional to the first power of the wall thickness [61]. When the wall thickness h is relatively very small, the extensional rigidity dominates the behavior of a thin shell. The flexural rigidity is only important where there are sharp changes in curvature. Therefore, the present Young's modulus is reduced by a factor of 10 in order to compensate the current membrane thickness of $50nm$. This approximation leads to the overall shear modulus value of $\mu_s h = 7.586 \times 10^{-6}N/m$, which is relatively close to the experimental upper value $6 \times 10^{-6}N/m$ in Yoon et al. [60] as well as the numerical value of $4.2 \times 10^{-6}N/m$ in both Pozrikidis [13] and Zhao et al. [4]. The present $50nm$ membrane thickness is also comparable with the work of Klöppel and Wall [31], where the red blood cell membrane is modelled as $40nm$ inner layer and $20nm$ outer lipid bilayer for a realistic mechanical behavior of human erythrocytes.

3.2 Boundary Conditions

The physical problem with the boundary conditions is illustrated in Figure 3.2 for a single red blood cell in a capillary. The fluid boundary conditions are set to the no-slip

Table 3.1 : Physical parameters for red blood cell and fluid plasma (pg : picogram).

Fluid	Density, ρ_f	$[pg/\mu m^3]$	1.025
	Dynamic viscosity, μ_f	$[pg/\mu m\mu s]$	1.1
	Maximum inflow velocity, U_{max}	$[\mu m/\mu s]$	0.001
Structure	Density, ρ_s	$[pg/\mu m^3]$	1.098
	Poisson ratio, ν_s	–	0.45
	Elasticity module, E	$[pg/\mu m\mu s^2]$	4.4

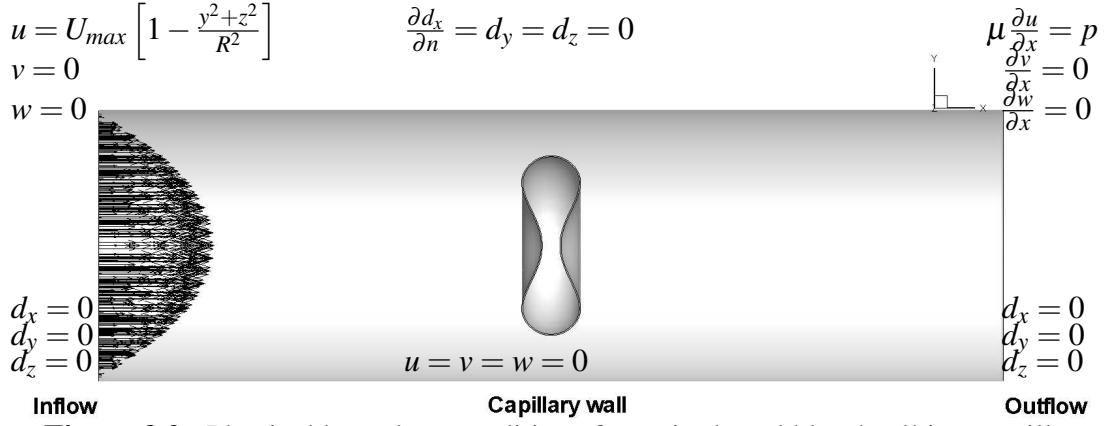


Figure 3.2 : Physical boundary conditions for a single red blood cell in a capillary tube.

boundary condition on the solid walls, the Dirichlet (paraboloid profile) velocity at the inlet, and the natural (traction-free) boundary condition at the outlet. Meanwhile, the displacement boundary conditions on the inlet and outlet are fixed to the zero Dirichlet condition. The displacement boundary conditions on the capillary wall are set to the homogeneous Neumann condition for the x -direction and the zero Dirichlet condition for the remaining y - and z -directions. The Neumann boundary condition ensures that the vertices on the capillary wall slide in the x -direction as the solid red blood cell membrane moves with the plasma flow. The mesh deformation algorithm within the fluid domain is based on the solution of the linear elasticity equations with modified coefficients [62]. The above kinematic and dynamic interface conditions are imposed at the fluid-solid interface corresponding to the inner and outer surfaces of the red blood cell membrane. It should be noted that there is no Dirichlet boundary condition for the solid red cell membrane and it is free to move and rotate due to the applied fluid forces on the interface. The present numerical calculations are started impulsively from the rest and solved in a time-accurate manner by marching in time with a fixed time step.



4. TWO-DIMENSIONAL NUMERICAL RESULTS

The first numerical simulations correspond to the two-dimensional simulation of a single red blood cells in a capillary. The height of the capillary channel is set to $15.6\mu m$ which is equal to two times of diameter of red blood cell. Single red blood cell in a channel with height of $15.6\mu m$ can be considered as benchmark case for this work. Spatial and temporal convergence are worked on this case. In addition, effect of different membrane thickness is also worked in a channel with height of $15.6\mu m$.

The calculations are carried out on three different meshes: coarse mesh M1, medium mesh M2 and fine mesh M3. The successive meshes are generated with DISTENE MeshGems-Hexa algorithm in three-dimensions based on the octree method by halving mesh size function. The initial meshes are created for a zero red cell membrane thickness. Then the radial basis function (RBF) based mesh deformation algorithm [50] is used to create the three-dimensional solid hexahedral elements with several layers by moving the vertices on the red cell membrane surface inwards with the distance equal to the solid membrane thickness. These conformal unstructured all-hexahedral meshes are used both two- and three-dimensional calculations. However, the slices on the $z = 0$ plane are extracted for the two-dimensional simulations as shown in Figure 4.1. The number of solid layers indicates the number of quadrilateral elements in the normal direction for the solid membrane. There are 4, 8 and 16 layers of solid quadrilateral elements on meshes M1 to M3, respectively, for the red blood cell membrane. The maximum aspect ratio of solid elements is set to 20. Δh_{min} and Δh_{max} represents the minimum and maximum mesh sizes, respectively. Coarse mesh M1 has 4,088 nodes and 3,923 elements, medium mesh M2 has 13,920 nodes and 13,611 elements and fine mesh M3 has 51,752 nodes and 51,139 elements for a channel with height of $15.6\mu m$. The details of the two-dimensional meshes are provided in Table 4.1.

The physical boundary conditions are set to no-slip boundary conditions on the solid walls, the Dirichlet (parabolic profile) velocity at the inlet and the natural (traction-free) boundary condition at the outlet. The maximum inlet velocity U_{max}

is set to $0.001\mu m/\mu s$. The capillary channel spans between $\pm 70\mu m$ where the initial undeformed red cell is located at the origin. The calculations are started from the rest and the time step is set to $100\mu s$. The non-dimensional Reynolds number ($Re = \rho_f U_{max} D / \mu_f$) is computed to be 0.007268 based on the plasma density ρ_f , the maximum inlet velocity U_{max} , the red cell diameter D and the plasma dynamic viscosity μ_f . The non-dimensional capillary number ($Ca = \mu_f U_{max} / \mu_s h$) is obtained to be 0.145 based on the shear modulus μ_s , the maximum inlet velocity U_{max} , the fluid dynamic viscosity μ_f and the membrane thickness h . Although the internal (cytoplasmic) fluid is assumed to be the same as the exterior suspending fluid (plasma), it does not effect the final red blood cell shape since the final cytoplasmic fluid has a constant velocity. However, this difference is important for white blood cells due to high viscosity difference [8]. For the solid membrane, Young's modulus is taken to be $4.4 kPa$ or $4.4 pg/\mu s^2 \mu m$ for a healthy red blood cell from previous experiments [6]. Although the membrane of RBC composed of several layer, the stiffness of RBC membranes is mainly dominated by the elasticity of the lipid bilayer which has approximately $5 nm$ thickness [6]. However, it is not possible reach this mesh resolution due to the resulting bad conditioned system for high aspect ratio solid elements. Therefore, the present Young's modulus is reduced by a factor of 10 in order to compensate the present membrane thickness of $50nm$ for the same membrane shear modulus value μh as well as the same Ca number.

4.1 Convergence Studies

The initial numerical calculations are used to establish the spatial and temporal convergence of the present numerical method. For this purpose, the single red cell simulations are carried on meshes M1–M3 with a time step of $100\mu s$ and the final red cell deformations at $t = 60ms$ are compared with each other in Figure 4.2-[a].

Table 4.1 : Computational meshes used for simulation of red blood cell for a channel height of $15.6\mu m$.

Mesh	Solid layers	Δh_{min}	Δh_{max}	Node number	Element number	DOF
M1	4	0.25	1	4,088	3,923	26,319
M2	8	0.125	0.5	13,920	13,611	89,215
M3	16	0.0625	0.25	51,752	51,139	330,471

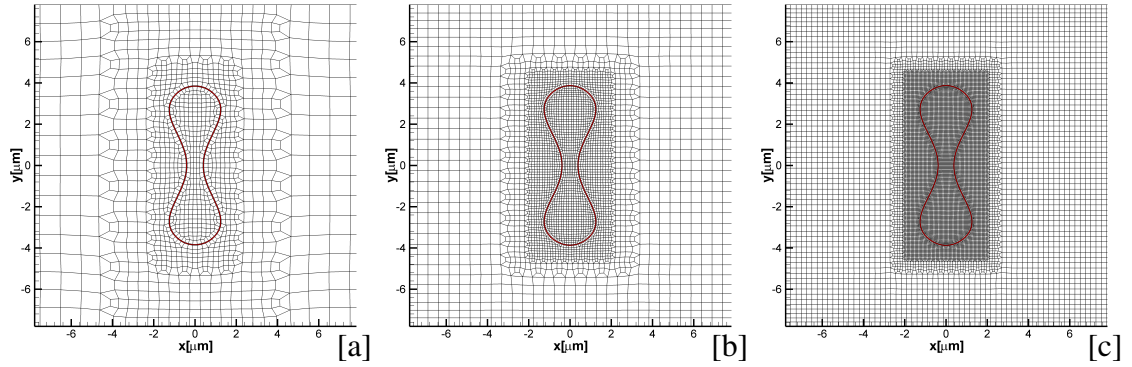


Figure 4.1 : Computational two-dimensional coarse mesh M1 [a], medium mesh M2 [b] and fine mesh M3 [c] for a single red blood cell in a channel with a height of $15.6\mu m$.

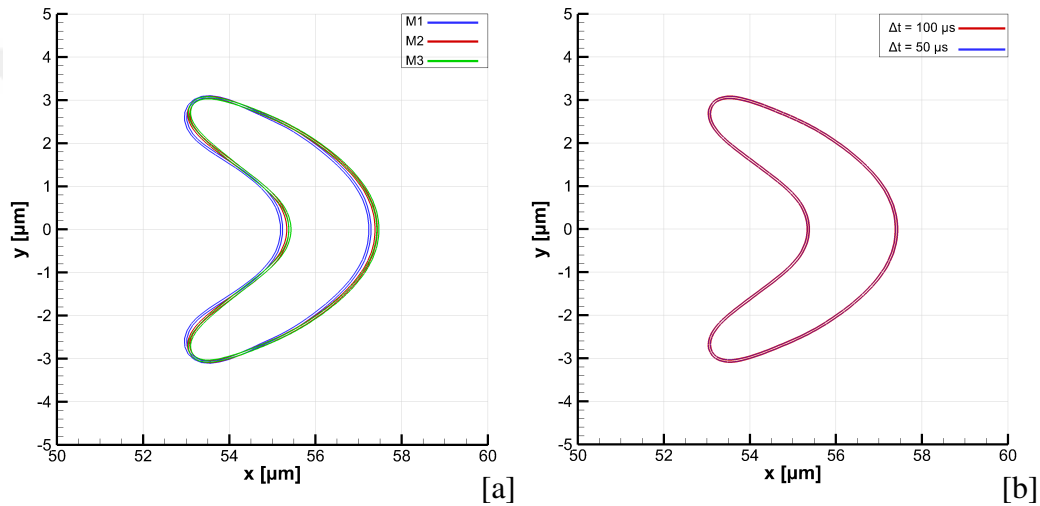


Figure 4.2 : Spatial convergence with $\Delta t = 100\mu s$ [a] and temporal convergence on mesh M2 [b] for a single red blood cell in a channel with a height of $15.6\mu m$ at $t = 60ms$.

The numerical results indicate that the results on meshes M2 and M3 are very similar to each other. Although the red cell shape on M1 is also very similar to others, it moves slightly slower. The reason is that we impose the analytic value of the velocity magnitude at the edge/face vertices at the inlet, which leads to a slightly lower average velocity throughout the capillary channel, since the mesh is relatively coarse at the inlet. The temporal convergence of numerical results is also investigated on mesh M2 at $t = 60ms$ by using $\Delta t = 50\mu s$ and $\Delta t = 100\mu s$ as shown in Figure 4.2-[b]. The comparison of the numerical results indicates that the results are indistinguishable from one another.

In addition to the spatial and temporal convergence studies, a convergence analysis is also carried out by changing the red cell membrane thickness as shown in Figure 4.3.

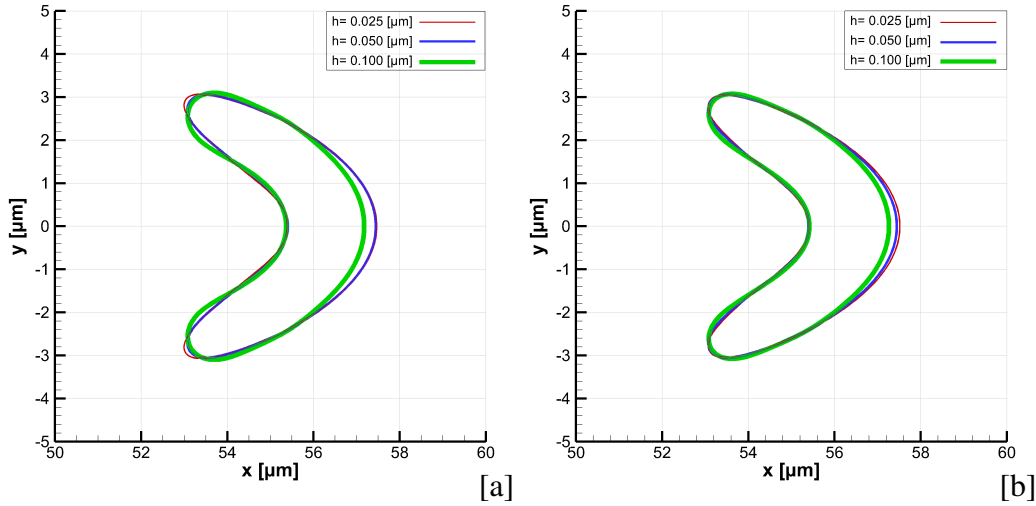


Figure 4.3 : Effect of different membrane thickness h using same shear modulus μ_s [a] and same membrane shear modulus $\mu_s h$ [b] to final red cell geometry at $t = 60ms$ in a channel with a height of $15.6\mu m$ at $t = 60ms$ on mesh M3.

As the red cell membrane thickness decreases for a constant shear modulus μ_s , the both flexural rigidity and extensional rigidity decrease and the red cell deforms more as seen in Figure 4.3-[a]. On the other hand, if the membrane thickness decreases for a constant overall shear modulus $\mu_s h$, the extensional rigidity stays constant while flexural rigidity decreases with the decrease in the thickness of the red cell membrane. When the wall thickness h is relatively very small, the extensional rigidity dominates the behavior of a red cell and the convergence of the deformed red cell membrane geometry can be seen in Figure 4.3-[b]. As it may be seen, the deformed geometries with the membrane thickness of $h = 50nm$ and $h = 25nm$ at $t = 60ms$ are almost identical.

4.2 Single Red Blood Cell in a Channel with Different Height

In order to demonstrate the importance of the fluid shear stress on the red cell deformation, the capillary channel heights are further reduced to $11.7\mu m$ and then $10\mu m$. The final deformed red cell geometries at $t = 60ms$ are provided in Figure 4.4 along with the computed contours of the u -velocity component within the capillary channel. The red cell deformation seems to be increased significantly with the decrease in channel height due to the increase in the fluid shear stress. The time variation of the red cell deformation and its movement are also provided in Figure 4.6 for the same channel heights. The cytoplasmic fluid within the red cell moves with a constant velocity when the steady state is reached and the velocity profile around the red cell is

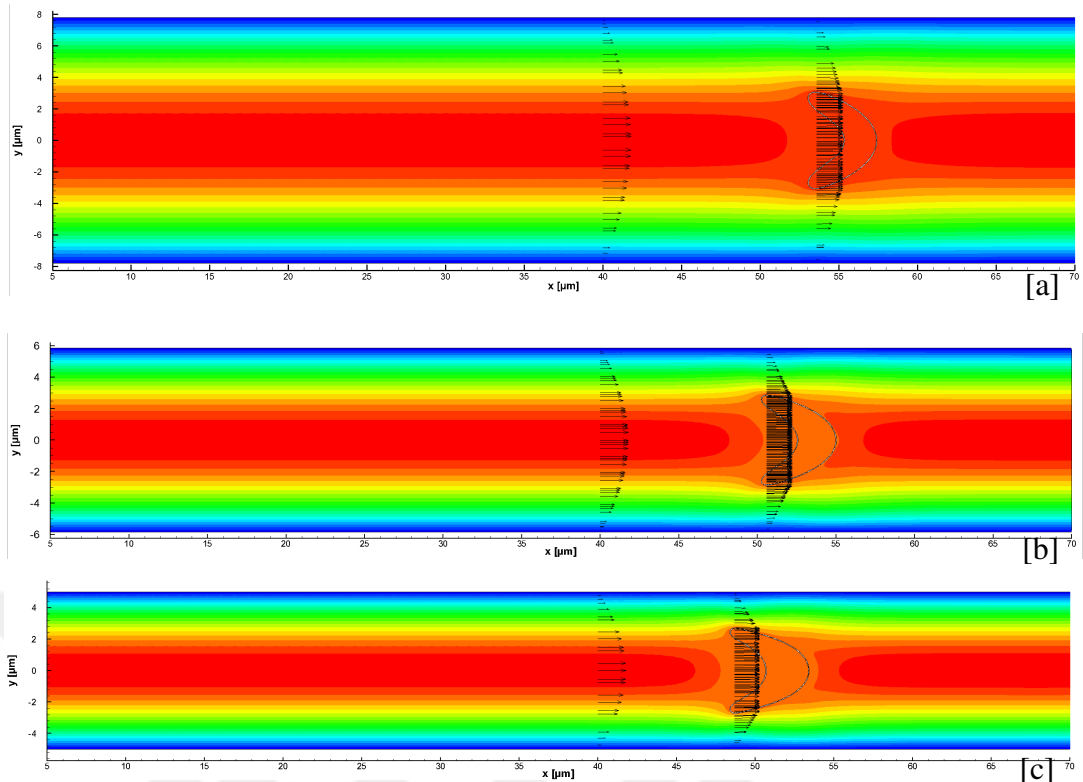


Figure 4.4 : Final positions/deformations at $t = 60ms$ with computed u -velocity component contours and velocity profiles at several different locations for a single red cell in a channel with a height of $15.6\mu m$ [a], $11.7\mu m$ [b] and $10\mu m$ [c] on mesh M3.

no longer parabolic, indicating a blunt velocity profile [20]. The blunt velocity profile with a relatively high velocity close to the vessel wall increases the flow resistance in the capillary due to the existence of the red blood cell.

Rigid and sickle cells have a larger constant velocity region in the blunt velocity profile and the flow resistance is further increased. This effect is particularly important for the

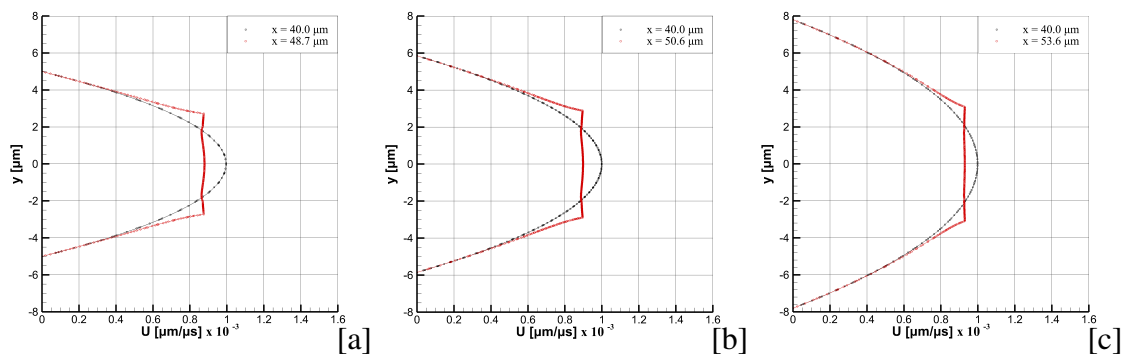


Figure 4.5 : Velocity profiles at $x = 40.0\mu m$ and the location corresponding to maximum red cell diameter at $t = 60ms$ in a channel with a height of $15.6\mu m$ [a], $11.7\mu m$ [b] and $10\mu m$ [c] on mesh M3.

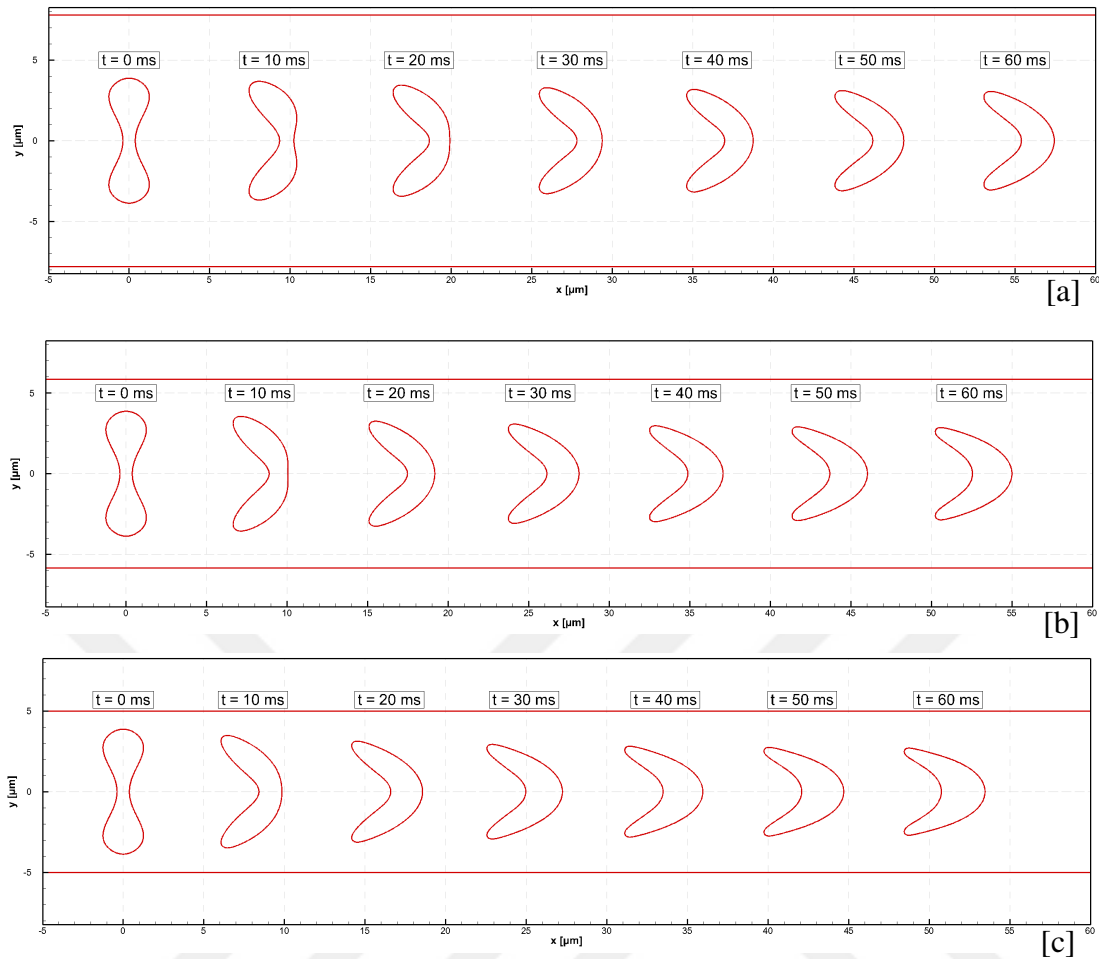


Figure 4.6 : Single red blood cell. Red blood cell positions/deformations at several different time levels for a channel height of $15.6\mu\text{m}$ [a], $11.7\mu\text{m}$ [b] and $10\mu\text{m}$ [c] on mesh M3.

array of the red blood cells in a capillary, where the red cells cause an increase in the shear rate on the capillary wall. The resistance becomes more severe for rather narrow capillaries. This phenomenon introduces non-Newtonian effects in capillaries even though the blood plasma itself is generally accepted as a Newtonian fluid. The pressure field within the red cell is also constant at the steady state in addition to the constant velocity value.

The red cell indicates a complex shape deformation in which the biconcave discoid shape changes to a parachute-like shape, which is convex in the front and concave at the rear. This deformation allows that the RBC successfully traverses through the capillary with the diameter smaller than that of undeformed RBC in microcirculation. The red cell deformations at several different time levels are superimposed on each other and the comparison is shown in Figure 4.7-[a]. The deformation of the red blood cell from the biconcave discoid shape to a parachute-like shape can be seen more clearly. In

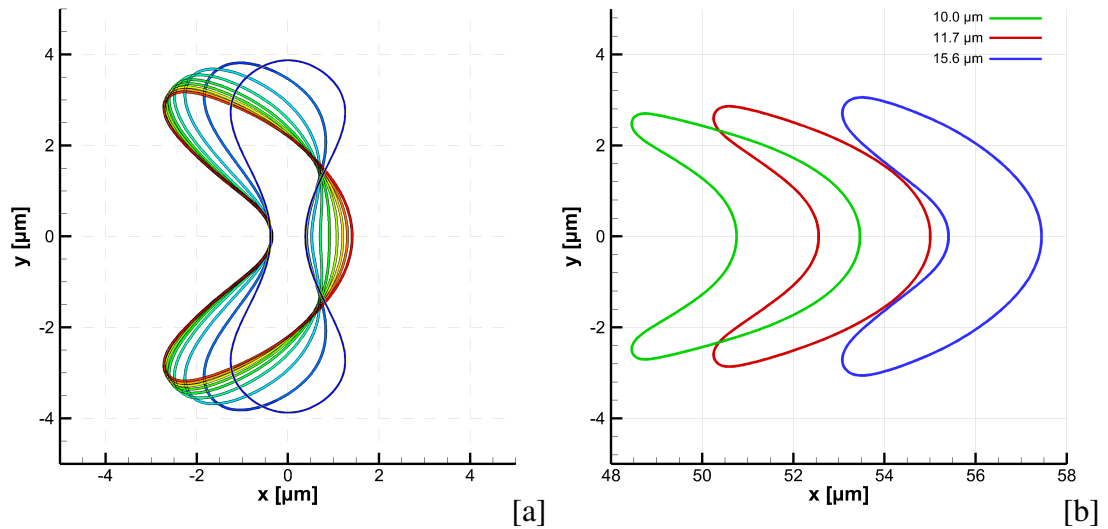


Figure 4.7 : Comparison of red blood cell deformations at several different time levels ($\Delta t = 5ms$) for a channel height of $15.6\mu m$ [a] and comparison of final cell geometry with results for several different channel heights at $t = 60ms$ [b] on mesh M3.

addition, the red cell translational velocity is found out to be reduced with the decrease in the channel height as seen in Figure 4.7-[b]. For the present cases, the solutions are found out to be symmetric according to the horizontal symmetry line.

4.3 Multiple Red Blood Cells in a Channel with a Height of $15.6\mu m$

Another important parameter for the hemorheology is the hematocrit ratio, which is the volume percentage of the red blood cells. This parameter is also related to the red cell spacing. The numerical calculations are carried out with five and nine red cells in a capillary channel with a height of $15.6\mu m$. The red cell spacing for the five cells case is set to $15.6\mu m$, meanwhile the spacing between the red cells is set to $7.8\mu m$ for the nine cells case. The final red cell deformations and the computed u -velocity component contours within the capillary are shown in Figure 4.8. For the present array of the red cells, the blunt velocity profiles around the red cells become more apparent. For the increase in the hematocrit ratio, the deformation and displacement of red blood cells are observed to be less compared to those of the single red cell case. The distance between the initial and final cells seems to be increased for the nine cells case compared to that of the five cells case. This indicates a slight increase in the cell spacing with the increase in the hematocrit ratio (a sort of diffusion effect).

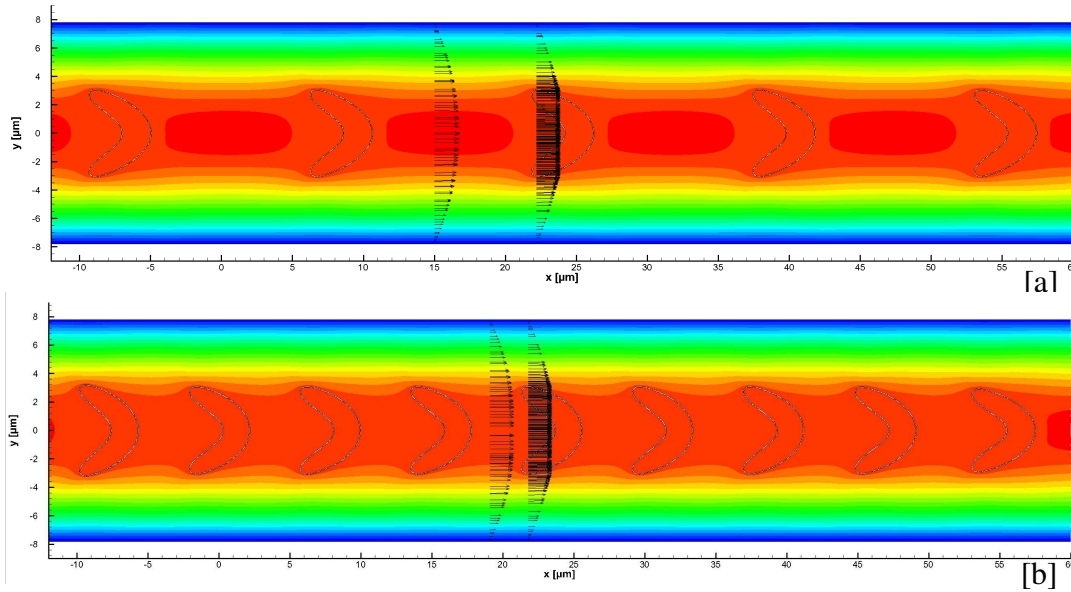


Figure 4.8 : Final positions/deformations at $t = 60ms$ with computed u -velocity component contours for 5 cells [a] and 9 cells [b] in a channel with a height of $15.6\mu m$ on mesh M3.

Shi et al. [63] also observed the same behavior in three-dimensions for the leading and trailing red cells and the authors contributed this behavior to short range hydrodynamic interactions, which leads to a larger deformation for the leading red cell and hence a higher translational velocity. The blunt velocity profile is more apparent not only on the red cell itself but also in the region between the red cells. This effect increases the flow resistance due to relatively high velocity close to the vessel wall. The wall vorticity divided by the wall vorticity for the planar Poiseuille flow is shown in Figure 4.9-[a] for the five and nine cell cases. As noted in Xiong and Zhang [64], the variation in the wall vorticity magnitude decreases as the cell hematocrit ratio is increased. The mean value of the wall vorticity is also increased as opposed to the work of Xiong and Zhang [64], where the authors imposed a constant pressure difference rather than a constant inflow velocity. Finally, the pressure values along the capillary channel symmetry line are also provided for different hematocrit ratios and capillary channel heights in Figure 4.9-[b]. The present hematocrit ratios for the channel height of $15.6\mu m$ have a slight effect on the pressure. There are several constant pressure regions for the cytoplasmic fluid, which is in accord with the constant velocity observed within the cells. There are also large constant pressure regions between the red cells in the case of nine cells. On the other hand, the channel width has a significant effect on the pressure variation along the symmetry line.

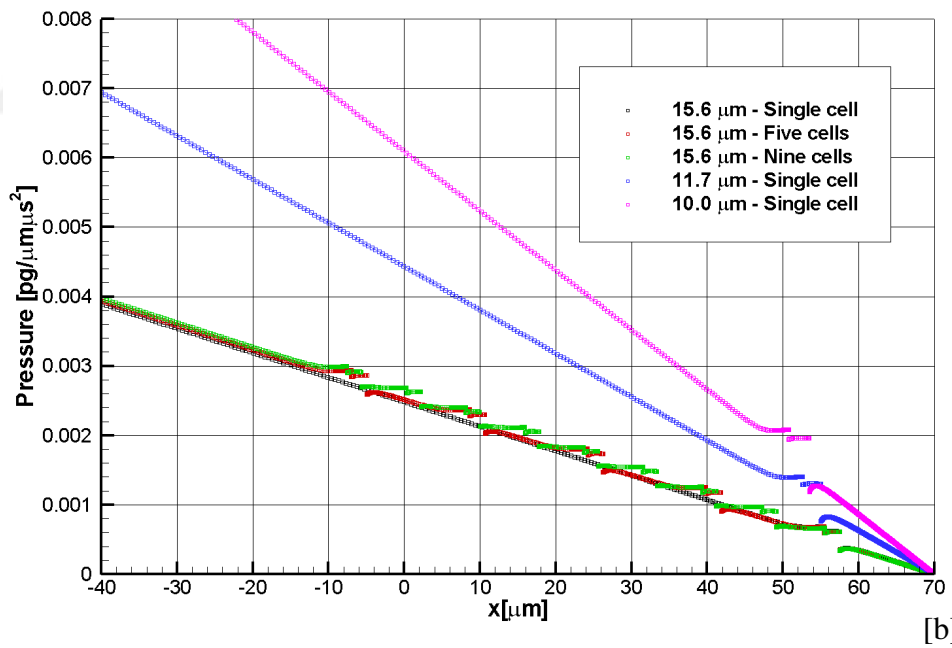
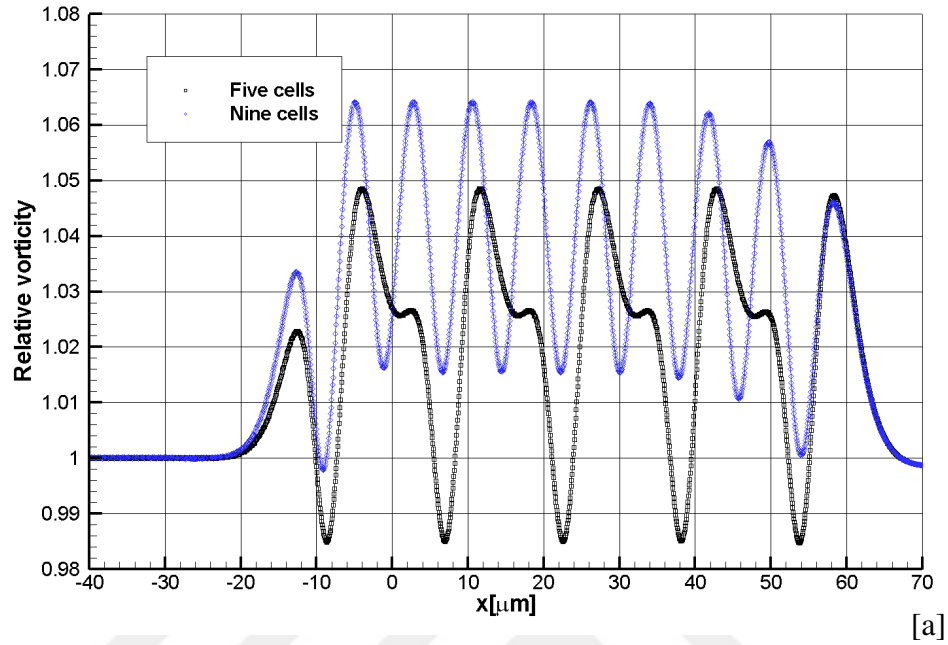


Figure 4.9 : Comparison of wall vorticity divided by the wall vorticity of planar Poiseuille flow for five and nine cells for a channel height of $15.6\mu\text{m}$ [a] and comparison of fluid pressure along the capillary channel symmetry line for different hematocrit ratios and capillary channel heights [b] at $t = 60\text{ms}$ on mesh M3.



5. THREE-DIMENSIONAL NUMERICAL RESULTS

The numerical simulations have been also carried out in three-dimensions by varying capillary tube diameter and red cell spacing. The diameter of the capillary tube is initially set to $15.6\mu m$. The three-dimensional successive meshes are generated with DISTENE MeshGems-Hexa algorithm based on the octree method by halving the mesh size function as mentioned before. The computational coarse mesh with 93,840 nodes and 88,331 hexahedral elements (1,064,685 DOF) is shown in Figure 5.1 in three-dimensions and the details of the meshes are provided in Table 5.1. The physical

Table 5.1 : Computational meshes used for simulation of red blood cell for a channel height of $15.6\mu m$.

Mesh	Solid layers	Δh_{min}	Δh_{max}	Node number	Element number	DOF
M1	4	0.25	1	93,840	88,331	1,064,685
M2	8	0.125	0.5	551,392	532,979	6,113,249
M3	16	0.0625	0.25	3,847,608	3,776,461	42,085,229

boundary conditions and the material properties are taken from the previous section. The capillary tube spans between $\pm 70\mu m$, where the red cell is initially located at the origin. The maximum velocity for the paraboloid inlet profile is again set to $0.01\mu m/\mu s$ in order to be consistent with the two-dimensional simulations. The

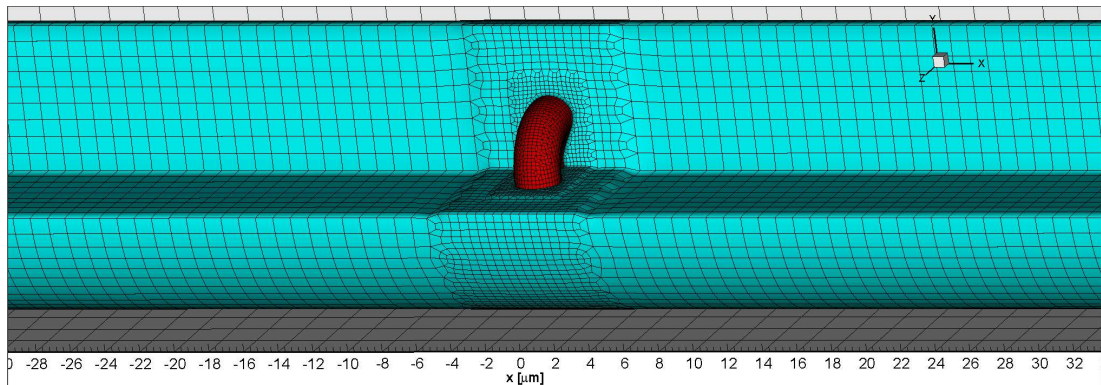


Figure 5.1 : Partial view of computational three-dimensional coarse mesh M1 with 93,840 nodes and 88,331 hexahedral elements for a single red blood cell in a capillary tube with a diameter of $15.6\mu m$.

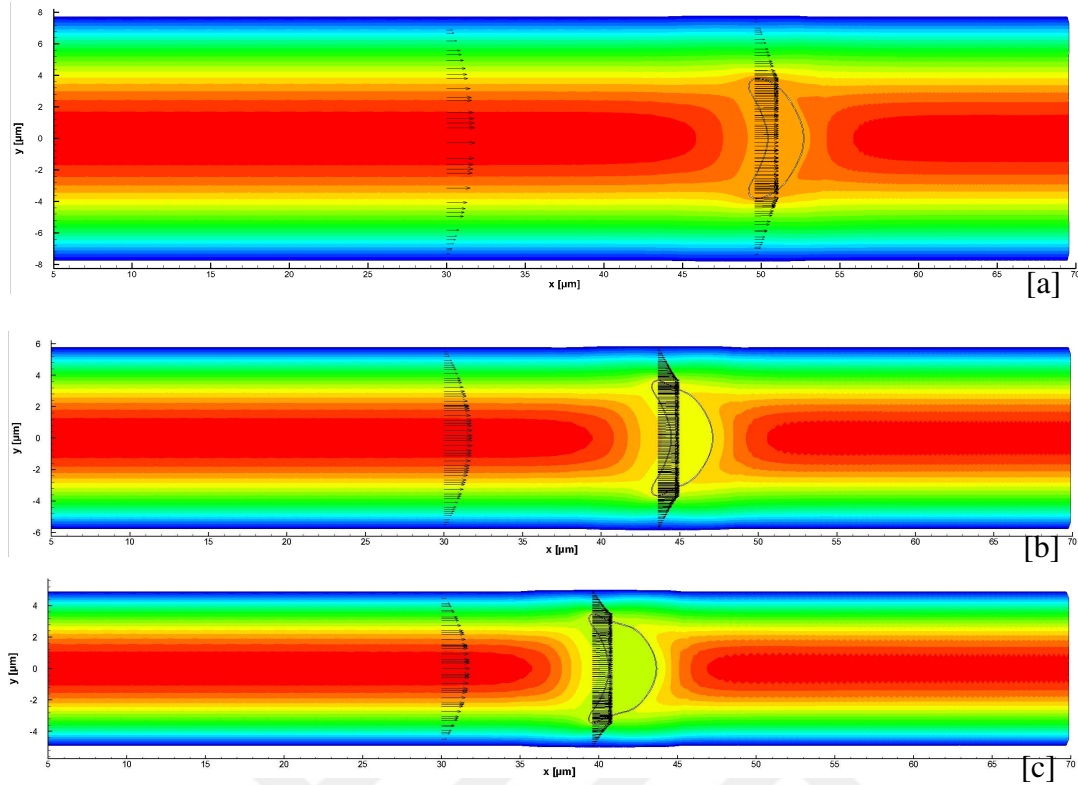


Figure 5.2 : Red blood cell positions/deformations with computed u -velocity component contours at $z = 0$ plane at $t = 60ms$ for a capillary tube diameter of $15.6\mu m$ [a], $11.7\mu m$ [b] and $10\mu m$ [c] on mesh M1.

calculations are started from the rest and the time step is set to $100\mu s$. The capillary tube diameters are further reduced to $11.7\mu m$ and then $10\mu m$ in order to see the effect of the increased fluid shear stress on the red cell deformation in three-dimensions. The computed contours of u -velocity component on $z = 0$ plane and the velocity profile around the red cell are provided in Figure 5.2 at $t = 60ms$ for different capillary tube diameters. As the tube diameter decreases, the red cell deforms more due to

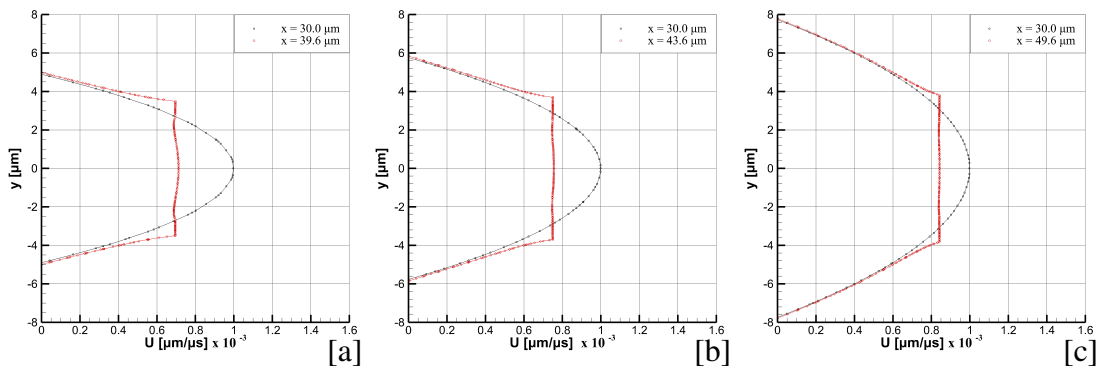


Figure 5.3 : Velocity profiles at $x = 30.0\mu m$ and the location corresponding to maximum red cell diameter at $t = 60ms$ in a channel with a height of $15.6\mu m$ [a], $11.7\mu m$ [b] and $10\mu m$ [c] on mesh M1.

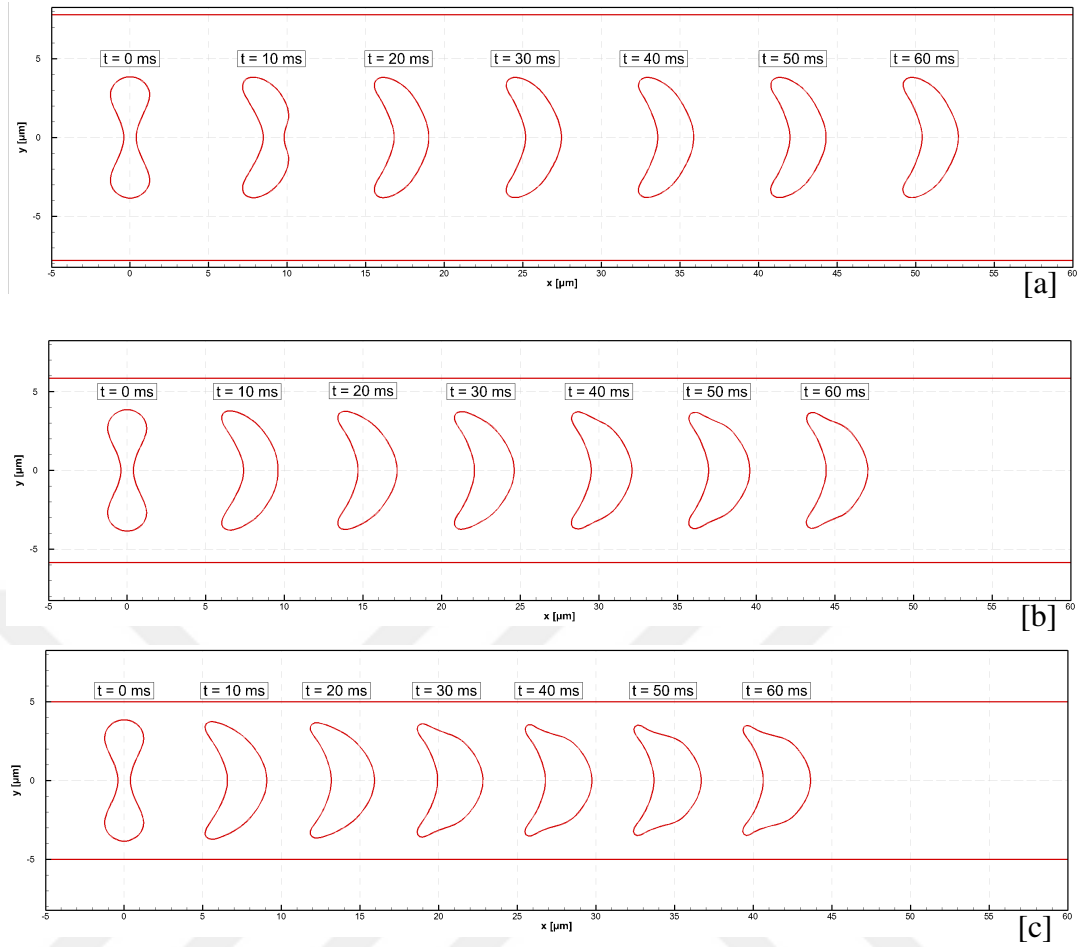


Figure 5.4 : Red blood cell positions/deformations at several different time levels for a single red blood cell in a capillary tube with a diameter of $15.6\mu m$ [a], $11.7\mu m$ [b] and $10\mu m$ [c] on mesh M1.

the increased fluid shear stress. Velocity profile at $x = 30.0\mu m$ and the location corresponding to maximum red cell diameter at $t = 60ms$ in a channel with height of $15.6\mu m$ [a], $11.7\mu m$ [b] and $10\mu m$ [c] are shown in Figure 5.3. The graphics proves that the red cells move with a constant velocity at the steady state condition. In case of three dimensions, the blunt velocity profile around the red cell is also more apparent. In addition, the red cell translational velocity is also found out to be significantly reduced with the decrease in the tube diameter as seen in the graphics. The time variations of the red cell deformation and its movement at several different time levels are provided in Figure 5.4 on $z = 0$ plane. The three-dimensional views of the same time levels are also provided in Figure 5.5. The numerical simulations indicate a complex shape deformation in which the biconcave discoid shape changes to a parachute-like shape as in two-dimensions. Surprisingly, as the capillary tube diameter is reduced to $11.7\mu m$ and $10\mu m$, the red cell undergoes a cupcake shaped buckling instability

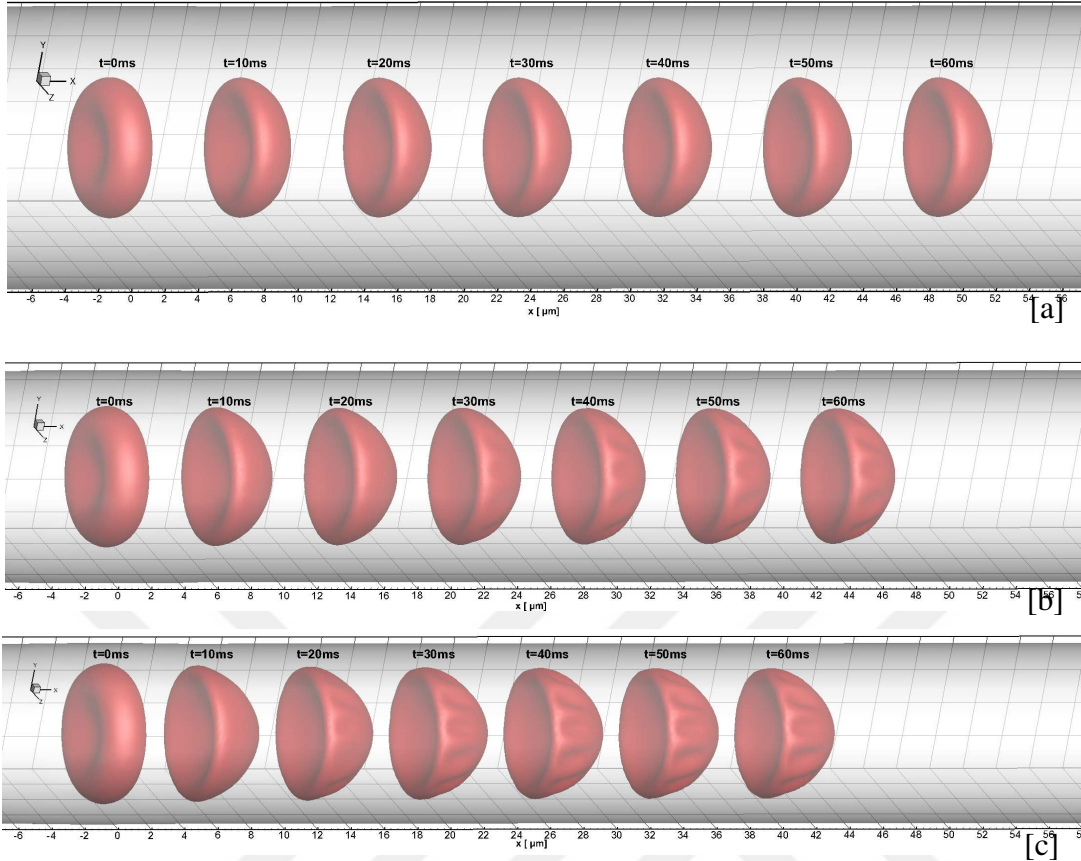


Figure 5.5 : Red blood cell positions/deformations at several different time levels for a single red blood cell in a capillary tube with a diameter of $15.6\mu m$ [a], $11.7\mu m$ [b] and $10\mu m$ [c] on mesh M1.

in three-dimensions due to the compressive elastic tension forces along the red cell membrane surface and the resulting red cell geometry is no longer axisymmetric but three-dimensional.

To the best of our knowledge, the present cupcake shaped buckling instability in small capillary tubes has not been noticed in three-dimensional simulations in the literature (see, for example, [4, 5]). One possibility may be the lack of sufficient initial random disturbances, which leads to a buckling instability due to the amplification of these random disturbances. This is particularly important for spectral type approaches as in Zhao et al. [4]. The second possibility is that Skalak et al. [42] law applied to the spherical capsule buckling produces a wider stability interval than the neo-Hookean law due to its strain hardening nature [48]. The present Saint Venant-Kirchhoff constitutive law does not show strain hardening property in the case of the compression of a body to zero volume, where the stress approaches zero instead of infinity. The main reason for such behavior is the lack of rank-one convexity [65] which implies non-polyconvexity

and the physically incorrect behavior of the stored energy function. Therefore, the existence of the underlying boundary value problem is not guaranteed at large strains [66]. However, the Saint Venant-Kirchhoff model can be applied successfully in the small strain-large displacement regime (such as beams and shells) which is in accord with the three-dimensional solid shell elements used for the RBC membrane. The third possibility is that the present bending stiffness value is relatively lower compared to the values used in the classical membrane models. Another possibility is that the wavenumber in the azimuthal direction may increase significantly with the decrease in the membrane thickness and the required mesh resolution may be underestimated in this direction. This high wavenumber could be seen in the experiment work of Hu et al. [44] for a spherical fluid-filled capsule undergoing a buckling instability as it passes through a circular tube with a diameter less than that of the capsule. In the literature, the buckling behavior of red cells has been observed only in the case of a red cell passing through a very narrow neck [4] and a red cell in simple shear flow [23] as well as at the cell-cell interface for the aggregation of red blood cells [43]. The similar formation of the rib-like buckling features are observed experimentally in Figure 6-D of Lee and Fung [67], where the authors modelled the deformation of a red blood cell in a capillary vessel by using flexible thin-walled rubber models suspended in a circular tube filled with a silicone fluid. The rubber models were also fluid-filled and geometrically similar to human red blood cell. Furthermore, the present cupcake shaped buckling instability is quite similar to the buckling of a half spherical shell subjected to an external pressure as seen in Lai and Liu [68].

The red cell deformations at several different time levels are superimposed on each other for a tube diameter of $15.6\mu m$ and the comparison is shown in Figure 5.6-[a]. The deformation of the red blood cell from the biconcave discoid shape to a parachute-like shape can be seen more clearly. The transition to parachute shape decreases the flow resistance. However, no buckling instability is observed for the tube diameter of $15.6\mu m$. The change in the red cell deformation is increased with the decrease in the capillary tube diameter. The red cell translational velocity is also found out to be significantly reduced with the decrease in the tube diameter as seen in Figure 5.6-[b]. In addition, as the tube diameter is decreased, the red cell membrane deforms more. However, this deformation is less compared to the decrease in the tube diameter.

Therefore, the red cell location corresponds to the slower moving plasma, which leads to a lower velocity even though the average velocity is same within the capillary tube in all cases. The three-dimensional numerical results also indicate that there is a significant decrease in the red cell deformation as seen in Figure 5.7 compared to that of the two-dimensional simulation. The significant decrease in the red cell deformation in three-dimensions is attributed to the three-dimensional red cell geometry, which can support larger structural loads. The smaller deformation in three-dimensions leads to a lower translational velocity for the red cell due to its position corresponding to the slower moving part of the plasma within the capillary tube, which leads to a larger constant velocity region in the blunt velocity profile. In addition, the average velocity within the capillary tube is $0.5U_{max}$ in three-dimensions rather than $0.6\bar{U}_{max}$ in two-dimensions. The average red cell membrane velocities are computed to be $0.00093\mu m/\mu s$ in two-dimensions and $0.00084\mu m/\mu s$ in three dimensions at $t = 60ms$ for a channel height/capillary tube diameter of $15.6\mu m$. These velocity values are significantly higher than the average plasma velocities, which are in accord with the experimental observation of Fåhræus [15]. In the literature, Fåhræus also observed that the red blood cells tend to accumulate at the higher velocity region of the flow field in a microvessel and their transit time through a tube is shorter on average than that of

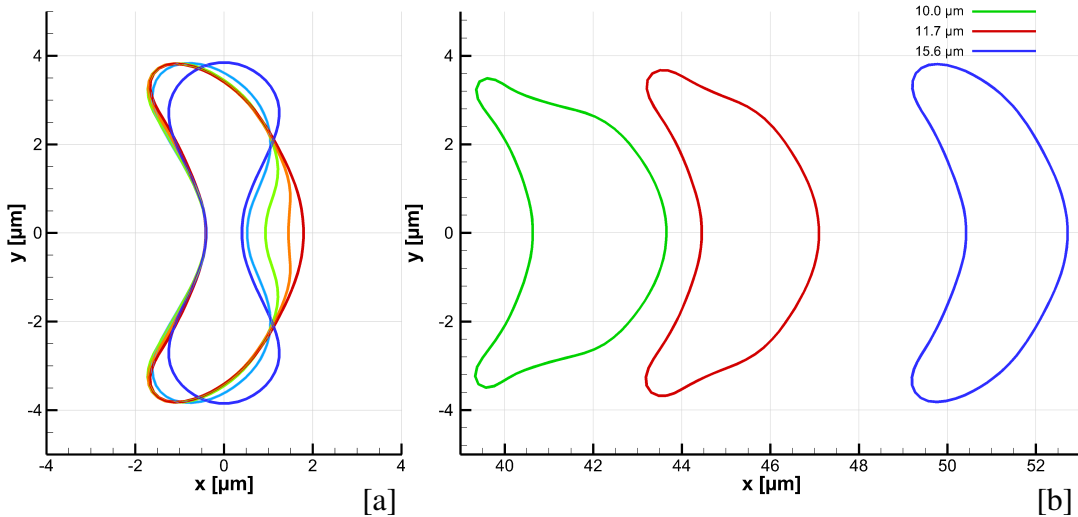


Figure 5.6 : Time-variation of red blood cell deformations at $z = 0$ plane at several different time levels ($\Delta t = 10ms$) [a], comparison of final cell geometry at $t = 60ms$ for several different tube diameters [b] on mesh M1.

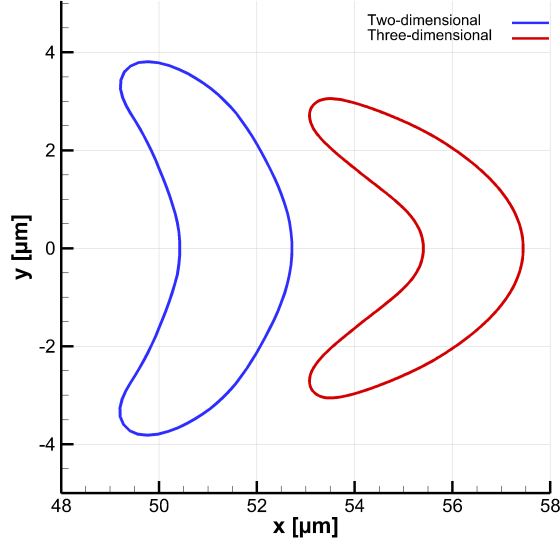


Figure 5.7 : Comparison of deformations in two- and three-dimensions at $t = 60ms$ for a channel height/tube diameter of $15.6\mu m$ [c] on mesh M1.

the plasma leading to a lower hematocrit ratio within the capillary tube compared to the hematocrit of the fluid exiting the tube, which is known as the Fåhræus effect [15].

The minimum thickness of the red cell T_1 is also significantly increased in three-dimensions for the tube diameter of $10\mu m$. In order to demonstrate the exact mass conservation property of the present FSI algorithm, the initial discrete volume of the cytoplasmic fluid is computed on mesh M1 for a capillary tube diameter of $10\mu m$ and its value is $85.256393560716617\mu m^3$. The final discrete volume at $t = 60ms$ is calculated to be $85.256393560834127\mu m^3$. Therefore, the exact mass conservation can be achieved at machine precision (11 digits) keeping in mind that the solver tolerance to proceed to next time step is set to 1×10^{-10} . The spatial convergence of the cupcake shaped membrane buckling instability is provided in Figure 5.8 for a capillary tube diameter of $10\mu m$ on meshes M1 to M3. The buckling instability forms thin rib-like features and the deformation is not axisymmetric but three-dimensional. The number of thin rib-like features is 12 on mesh M1 and these structures are uniformly distributed in the azimuthal direction. The number of these structures is increased to 14 on mesh M2 and the structures show slight uneven distribution in the azimuthal direction probably depending on the initial disturbances. The number of the thin rib-like features is further increased to 17 on mesh M3 indicating relatively high wavenumber similar to that of the spherical fluid-filled capsules in Hu et al. [44].

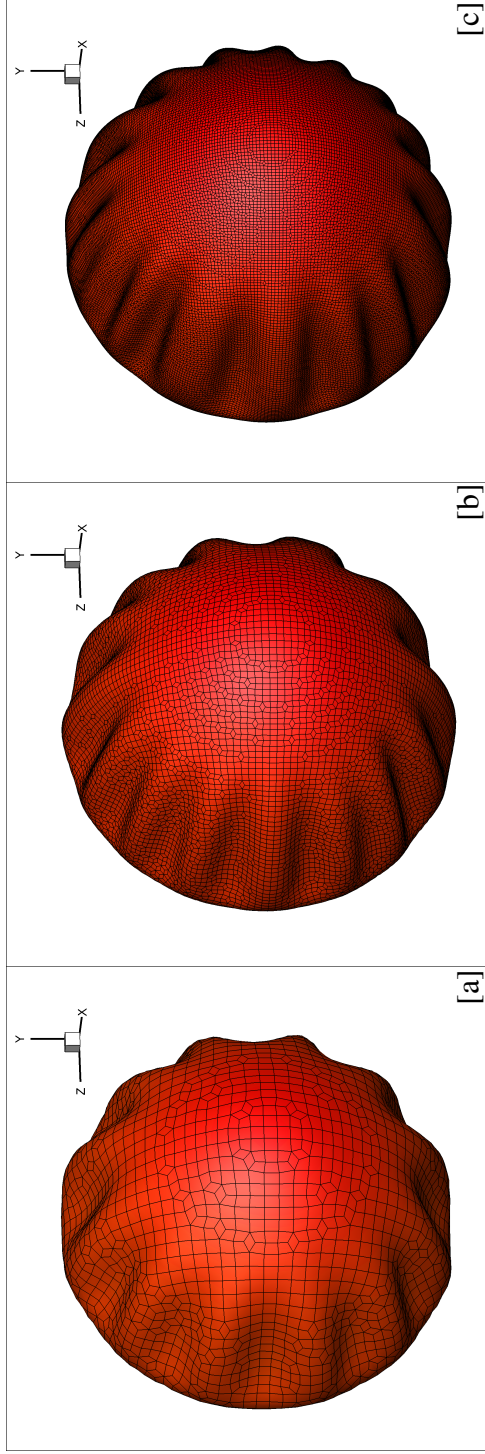


Figure 5.8 : Mesh convergence of cupcake shaped membrane buckling instability on mesh M1 [a], mesh M2 [b] and mesh M3 [c] for a capillary tube diameter of $10\mu\text{m}$ at $t = 60\text{ms}$.

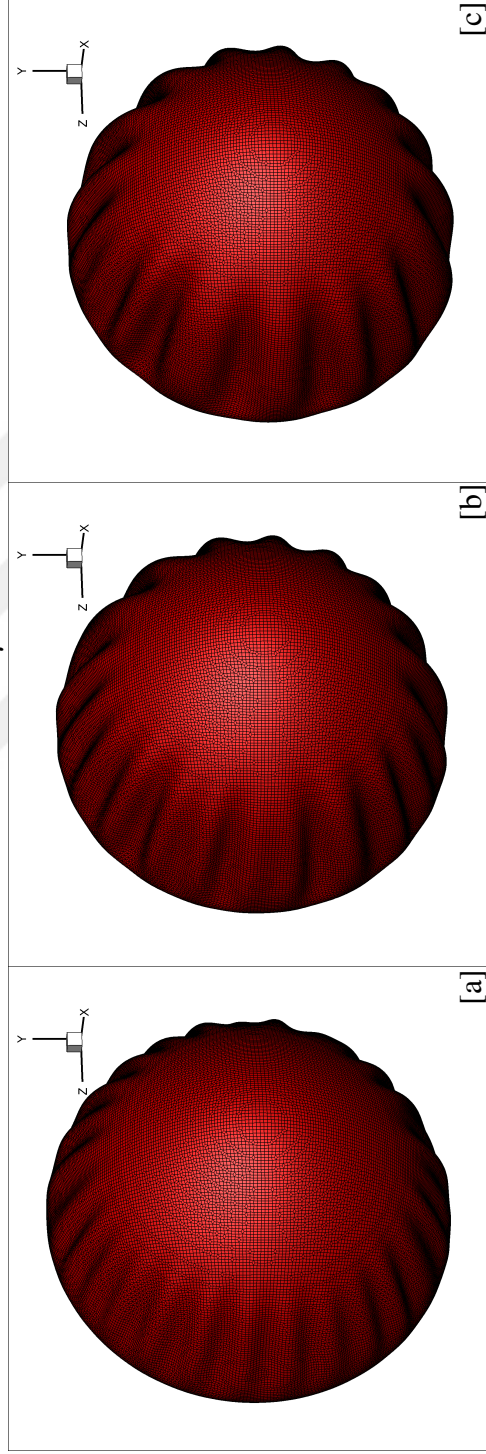


Figure 5.9 : Time evolution of cupcake shaped membrane buckling instability on mesh M3 at $t = 20\text{ms}$ [a], $t = 40\text{ms}$ [b] and $t = 60\text{ms}$ [c] for a capillary tube diameter of $10\mu\text{m}$.

In this case, there are 47,342 quadrilateral elements on the red cell membrane outer/inner surface in order to resolve the wavenumber of the buckling instability, which leads to a relatively large FSI simulation with 29,090,781 DOF. The spherical fluid-filled capsule deformed in axisymmetric elongational flow also indicates the similar buckling instability [48]. However, the buckling on the red cell membrane leads to relatively more complex instability due to its initial biconcave discoid shape compared to that of the oblate spheroidal capsule [23]. The experimental work of Risso et al. [45] indicates that the spherical capsules in a circular tube with the blockage ratios and the capillary numbers close to the present values leads to a relatively simple buckling, where the trailing end buckles inward with the leading pole moving away from the centre. Actually, this simple behavior is more similar to the outward buckling of the red cell membrane leading part rather than the formation of the rib-like features. The present wavenumber of the buckling instability is even higher during the initial formation of the buckling with more uniform distribution and the rib-like features tend to merge with the increased deformation, forming larger structures as seen in Figure 5.9. Therefore, the post-buckling behavior of the red cell membrane is highly unstable and non-linear, which is in accord with the observations related to the spherical capsules [44]. The buckling instability is observed to happen where the membrane is subjected to the compressive stress as seen from the pressure contours in Figure 5.10. The buckling instability is observed to happen where the membrane is subjected to the compressive stress as seen from the pressure contours in Figure 5.10. The wall shear stress vectors and their streamtraces are also provided

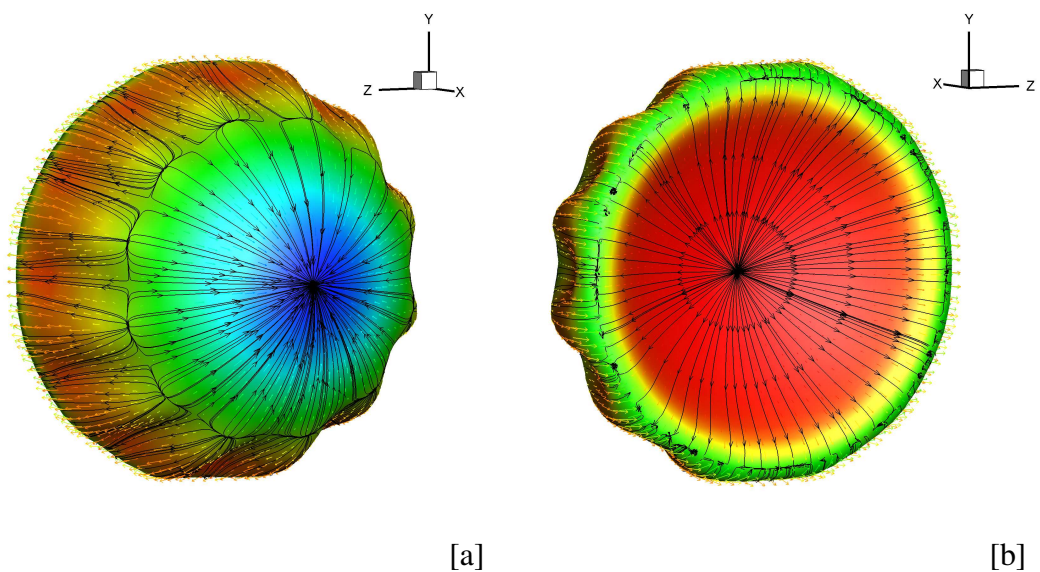


Figure 5.10 : Front [a] and back [b] views of wall shear stress vectors and their streamtraces along with pressure contours for a capillary tube diameter of $10.0\mu m$ at $t = 60ms$ on mesh M1.

in the same figure and the streamtraces indicate separation lines at the front and the back of the red cell. These separation lines can be easily seen if the streamlines are drawn with respect to the red cell held stationary while the tube moves to the left. The initial orientation of the red blood cell is also an important factor, which defines the final deformed shape [27]. The effect of the initial red cell orientation to the final deformation is investigated when the symmetry axis of the red cell lies parallel to the flow direction as shown in Figure 5.11. The calculation indicates a completely different red cell deformation, which is in accord with the Figure 14 of Hashemi and Rahnama [27]. For the present red cell orientation, the red cell moves faster, since its location corresponds to the higher velocity region of the plasma within the capillary tube.

The three dimensional simulations are also carried out for five and nine cells in order to investigate the effect of the cell spacing (hematocrit) in three-dimensions as well as the cell-cell interactions. The red cell spacing for the five cells case is set to $15.6\mu m$, meanwhile the spacing between the red cells is set to $7.8\mu m$ for nine cells case. The computational mesh for the nine cell case leads to 557,080 nodes and 543,495 hexahedral elements leading to 6,185,417 DOF. The computed red cell deformations at $t = 60ms$ are shown in Figure 5.12 for a capillary tube diameter of $15.6\mu m$. The red cells move with a constant velocity at the steady state and the blunt velocity profile is more profound for the array of the red cells, which introduces an increase in the apparent viscosity compared that of the plasma, causing non-Newtonian effects in capillaries. The blunt velocity region is larger compared to that of the two dimensional case, since the red cells deform less in three-dimensions. The deformation of the leading red cell is observed to be larger compared to the other cells and its velocity

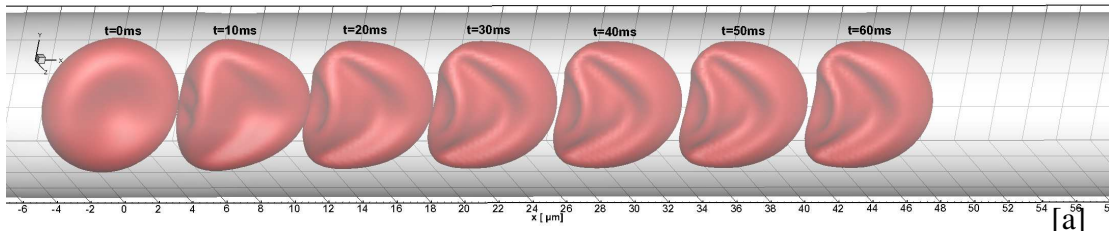


Figure 5.11 : Effect of initial orientation on red cell positions/deformations at several different time levels for a single red blood cell in a capillary tube with a diameter of $10\mu m$ [c] on mesh M1.

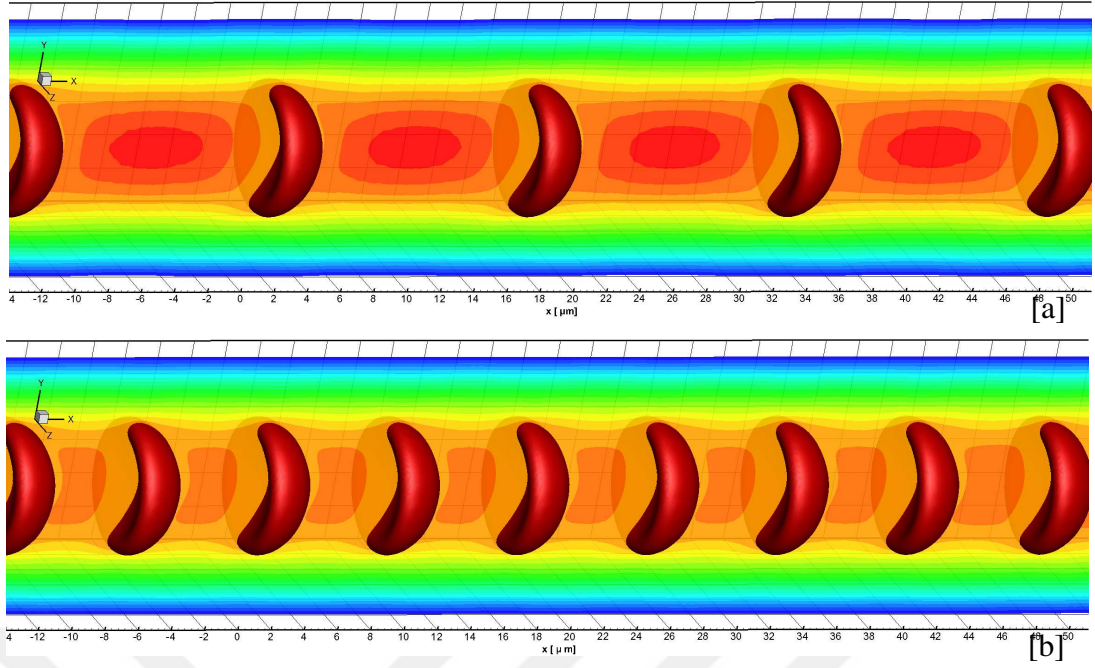


Figure 5.12 : Effects of hematocrit density using five red cells [a] and nine red cells [b] on u -velocity on $z = 0$ plane and deformations for a capillary tube diameter of $15.6\mu m$ at $t = 60ms$ on mesh M1.

is slightly higher. The single red cell in a capillary moves slightly faster compared to the nine-cells.

It is rather difficult to validate the present results due to the fact that the numerical results in the literature are obtained using different membrane constitutive laws (e.g., [42]), where the membrane thickness is zero. Nevertheless, the numerical validation case used in Pozrikidis [13], Zhao et al. [4] and Shi et al. [5] has been carried out for a periodic array of red cells in a narrow capillary tube. For this benchmark problem, the capillary tube diameter is set to $9.024\mu m$ and the distance L between the red cells is equal to $5.64\mu m$. The mean inlet velocity is taken to be $0.3525mm/s$, the membrane overall shear modulus $\mu_s h$ is $4.2 \times 10^{-6} N/m$ and the plasma dynamic viscosity is $1.2 \times 10^{-3} kg/ms$. The membrane thickness is set to $50nm$ as before. The convective and time derivative parts of the incompressible Navier-Stokes equation are neglected in order to be consistent with the Stokes solution of Zhao et al. [4]. The capillary number based on the mean inlet velocity is computed to be 0.1007. The periodic boundary conditions between the inlet and outlet are imposed for the velocity vector $\mathbf{u}(x, y, z) = \mathbf{u}(x + L, y, z)$, the displacement vector $\mathbf{d}(x, y, z) = \mathbf{d}(x + L, y, z)$ and the pressure $p(x, y, z) = p(x + L, y, z) + \Delta p$, where the pressure jump value Δp is computed implicitly from the imposed average mass flow rate [69].

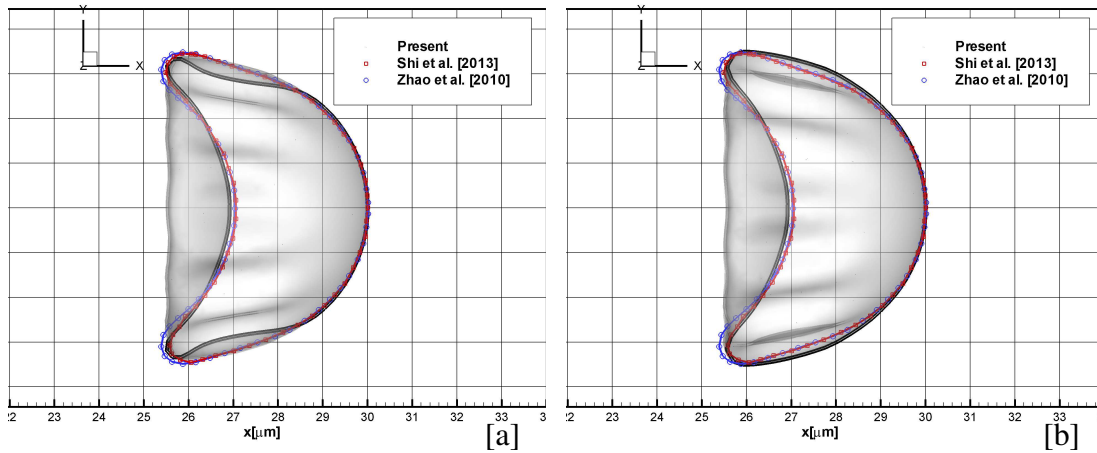


Figure 5.13 : Comparison of three-dimensional red cell membrane geometry corresponding to maximum indentation [a] and protrusion [b] with the results of Zhao et al. [4] and Shi et al. [5] for a capillary tube diameter of $9.024\mu m$ at $t = 60ms$.

The initial mesh M1 generated with DISTENE MeshGems-Hexa algorithm consists of 50,880 nodes and 47,615 elements. The numerical simulation for the present capillary tube diameter leads to the membrane buckling instability and the comparisons of the computed red cell geometry corresponding to the maximum indentation and protrusion at $t = 60ms$ are provided in Figure 5.13. The overall red cell deformation is similar to the results of Zhao et al. [4] and Shi et al. [5]. The deformation index, which is defined as the maximum red cell length divided by its maximum diameter [5], is calculated to be 0.645. Although the present deformation index is slightly lower due to the protrusion region on the membrane surface as seen in Figure 5.13-[b], the average deformation is increased due the membrane buckling, which leads to an increase in the red cell thickness T_1 . The deformed red cell membrane is also observed to be slightly thinner in the front ($44nm$) and thicker in the back ($49nm$), which is not considered in the classical membrane models. The deformation index for a single red cell in a long capillary tube ($140\mu m$) with the same diameter is computed to be 0.717, which is relatively in a better agreement with the experimental results of Tsukada et al. [70]. In the present numerical simulations, we have noted that the buckling instability is delayed significantly on partially axisymmetric meshes. A new partially axisymmetric mesh M1 with 67,361 nodes and 64,640 elements is created by using CUBIT mesh generation environment [71] and the solid mesh vertices corresponding to the buckling region are computed by uniformly sweeping the grid points in the azimuthal direction.

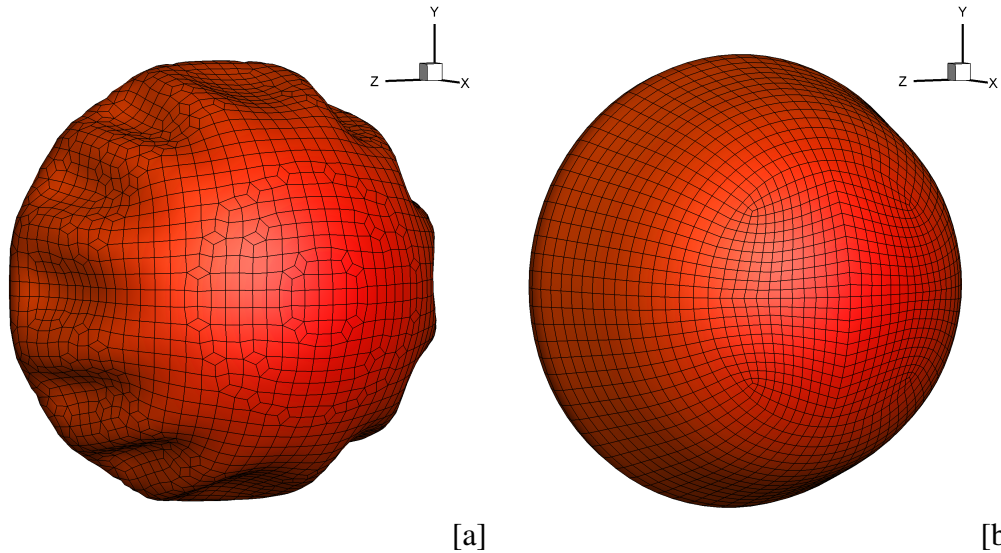


Figure 5.14 : Effect of computational mesh to development of buckling for a capillary tube diameter of $9.024\mu m$ at $t = 40ms$: Initial unstructured mesh M1 [a] and partially axisymmetric mesh M1 [b].

The developments of the three-dimensional red cell membrane buckling instabilities on both computational meshes are provided in Figure 5.14 at $t = 40ms$. The buckling instability on the partially axisymmetric mesh M1 is not apparent at $t = 40ms$ and it takes relatively longer to reach the final buckled shape. The larger deformation on the initial unstructured mesh M1 leads to a lower flow resistance and a slightly higher red cell translational velocity. However, we can not create a fully axisymmetric mesh, since it requires to use prismatic elements corresponding to the polar singularity along the x -axis, which is not supported with the current algorithm. Therefore, the lack of sufficient small random initial disturbances or the lack of the numerical simulation time may be the reason why the early numerical results did not observe the present buckling instability. Nevertheless, this still should be confirmed by using other constitutive laws in three-dimensions. In the present simulations, the red cell membrane thickness is also increased to $100nm$, which is the maximum red cell blood cell membrane thickness [29], in order to increase the membrane bending stiffness (8 times) while keeping the membrane shear modulus μ_s the same. Although this also doubles the membrane overall shear modulus, the simulation shows that the red cell membrane buckling still persists.



6. CONCLUSION

The parallel fully coupled (monolithic) fluid-structure interaction approach [35,36] has been applied to investigate the deformation of red blood cells in capillaries, where cell deformability has significant effects on blood rheology. The present numerical method in fluid domain is based on Arbitrary Lagrangian-Eulerian (ALE) formulation with the stable arrangement of primitive variables [50], meanwhile the classical Galerkin finite element formulation in a Lagrangian frame is used in the solid domain. The numerical method employs conformal hexahedral elements at the fluid-solid interface in order to accurately resolve the sharp gradients at the interface. In addition, the local and global geometric conservation laws (DGCL) [37] are satisfied at discrete level and the compatible kinematic boundary condition [36] is enforced at the interface between the solid and fluid domains in order to conserve the mass of the cytoplasmic fluid within the red cell at machine precision. Furthermore, the new projection type approximate block preconditioner is proposed and the parallel algebraic multigrid solver BoomerAMG is used for the scaled discrete Laplacian provided by the HYPRE library [40] which we access through the PETSc library [41]. Three important physical parameters for the blood flow are simulated and analyzed: (i) the effect of capillary diameter, (ii) the effect of red cell membrane thickness and (iii) the effect of red cell spacing (hematocrit). The capillary diameter is found out to be particularly important for the flow pressure gradient as well as the deformation of red blood cells. The results also show that the cell deformation decreases with increasing hematocrit density, which is also shown to play a significant role for velocity field. In the present simulations, the three dimensional red cell membrane, which is at the order of $40 - 50nm$ [59], is modelled using the three-dimensional solid shell elements rather than the two-dimensional membrane elements with zero thickness and the numerical simulations indicate significant thinning of the red cell membrane in the leading/front part for large shear values, which is ignored in the classical membrane models. The thickness effects are particularly important to model bending moments and transverse shear forces in order to predict the post-buckling behavior [44]. The calculations also

show a complex shape deformation in which the biconcave discoid shape changes to a parachute-like shape which is in accord with the early results in the literature. In addition, the red cells in small capillaries undergo a cupcake shaped buckling instability forming thin rib-like features in three-dimensions due to the compressive elastic tension forces along the membrane surface and the resulting red cell geometry is no longer axisymmetric but three-dimensional. The wavenumber of the instability in the azimuthal direction is also relatively high and it is computationally challenging to resolve. To our best knowledge, the cupcake shaped buckling instability in small capillaries has not been noted in the literature. The present buckling mechanism may further ramifications to reduce the flow resistance in the microcirculation and alter the oxygenation of surrounding tissues in small capillaries due to its larger surface area next to the endothelium. Although we employ the simplest type of hyperelastic material model, the present numerical simulations revealed the most of the properties encountered in blood flows in a microcirculation. In the future, we will consider more realistic solid red cell membrane models as in the work of Klöppel and Wall [31]. In addition, the numerical algorithm requires local remeshing capability in the fluid domain for more complex deformations and cell-cell interactions.

REFERENCES

- [1] **Kim, Y., Kim, K. and Park, Y.** (2012). Measurement techniques for red blood cell deformability: recent advances, *Blood cell-An overview of studies in hematology*, InTech.
- [2] **Secomb, T.** (2003). Mechanics of red blood cells and blood flow in narrow tubes.
- [3] **Eken, A.**, A PARALLEL MONOLITHIC APPROACH FOR THE NUMERICAL SIMULATION OF FLUID-STRUCTURE INTERACTION PROBLEMS.
- [4] **Zhao, H., Isfahani, A.H., Olson, L.N. and Freund, J.B.** (2010). A spectral boundary integral method for flowing blood cells, *Journal of Computational Physics*, 229(10), 3726–3744.
- [5] **Shi, X., Lin, G., Zou, J. and Fedosov, D.A.** (2013). A lattice Boltzmann fictitious domain method for modeling red blood cell deformation and multiple-cell hydrodynamic interactions in flow, *International Journal for Numerical Methods in Fluids*, 72(8), 895–911.
- [6] **Kim, Y., Kim, K. and Park, Y.** (2012). *Measurement techniques for red blood cell deformability: Recent advances*, InTech.
- [7] **Eggleton, C.D. and Popel, A.S.** (1998). Large deformation of red blood cell ghosts in a simple shear flow, *Physics of Fluids*, 10(8), 1834–1845.
- [8] **Marella, S.V. and Udaykumar, H.S.** (2004). Computational analysis of the deformability of leukocytes modeled with viscous and elastic structural components, *Physics of Fluids*, 16, 244–264.
- [9] **Secomb, T.W.** (1987). Flow-dependent rheological properties of blood in capillaries, *Microvascular Research*, 34, 46–58.
- [10] **Peskin, C.S.** (1977). Numerical analysis of blood flow in the heart, *Journal of Computational Physics*, 25(3), 220–252.
- [11] **Liu, Y., Zhang, L., Wang, X. and Liu, W.K.** (2004). Coupling of Navier–Stokes equations with protein molecular dynamics and its application to hemodynamics, *International Journal for Numerical Methods in Fluids*, 46(12), 1237–1252.
- [12] **Liu, Y. and Liu, W.K.** (2006). Rheology of red blood cell aggregation by computer simulation, *Journal of Computational Physics*, 220(1), 139–154.
- [13] **Pozrikidis, C.** (2005). Axisymmetric motion of a file of red blood cells through capillaries, *Physics of Fluids*, 17(3), 031503.

- [14] **Zhang, J., Johnson, P.C. and Popel, A.S.** (2007). An immersed boundary lattice Boltzmann approach to simulate deformable liquid capsules and its application to microscopic blood flows, *Physical Biology*, 4(4), 285.
- [15] **Fåhræus, R.** (1928). Die Strömungsverhältnisse und die Verteilung der Blutzellen im Gefäßsystem. Zur Frage der Bedeutung der intravasculären Erythrocytenaggregation, *Klinische Wochenschrift*, 7, 100–106.
- [16] **Zhang, J., Johnson, P.C. and Popel, A.S.** (2008). Red blood cell aggregation and dissociation in shear flows simulated by lattice Boltzmann method, *Journal of Biomechanics*, 41(1), 47–55.
- [17] **Le, D.V., White, J., Peraire, J., Lim, K. and Khoo, B.** (2009). An implicit immersed boundary method for three-dimensional fluid-membrane interactions, *Journal of Computational Physics*, 228(22), 8427–8445.
- [18] **Hosseini, S.M. and Feng, J.J.** (2009). A particle-based model for the transport of erythrocytes in capillaries, *Chemical Engineering Science*, 64(22), 4488–4497.
- [19] **Hosseini, S.M. and Feng, J.J.** (2012). How malaria parasites reduce the deformability of infected red blood cells, *Biophysical Journal*, 103(1), 1–10.
- [20] **Wang, T. and Xing, Z.** (2010). Characterization of blood flow in capillaries by numerical simulation, *Journal of Modern Physics*, 1(06), 349.
- [21] **Ye, T., Li, H. and Lam, K.Y.** (2010). Modeling and simulation of microfluid effects on deformation behavior of a red blood cell in a capillary, *Microvascular Research*, 80, 453–463.
- [22] **Ye, T., Phan-Thien, N., Khoo, B.C. and Lim, C.T.** (2014). A file of red blood cells in tube flow: A three-dimensional numerical study, *Journal of Applied Physics*, 116, 124703.
- [23] **Huang, W.X., Chang, C.B. and Sung, H.J.** (2012). Three-dimensional simulation of elastic capsules in shear flow by the penalty immersed boundary method, *Journal of Computational Physics*, 231(8), 3340–3364.
- [24] **Reasor Jr, D.A., Clausen, J.R. and Aidun, C.K.** (2012). Coupling the lattice-Boltzmann and spectrin-link methods for the direct numerical simulation of cellular blood flow, *International Journal for Numerical Methods in Fluids*, 68, 767–781.
- [25] **Freund, J.B.** (2013). The flow of red blood cells through a narrow spleen-like slit, *Physics of Fluids*, 25(11), 110807.
- [26] **Chivuka, V., Mousel, J., Lu, J. and Vigmostad, S.** (2014). Micro-scale blood particulate dynamics using a non-uniform rational B-spline-based isogeometric analysis, *Int. J. Numer. Meth. Biomed. Engng.*, 30, 1437–1459.

- [27] **Hashemi, Z. and Rahnama, M.** (2016). Numerical simulation of transient dynamic behavior of healthy and hardened red blood cells in microcapillary flow, *International Journal for Numerical Methods in Biomedical Engineering*, 32(11).
- [28] **Balogh, P. and Bagchi, P.** (2017). A computational approach to modeling cellular-scale blood flow in complex geometry, *Journal of Computational Physics*, 334, 280–307.
- [29] **Freund, J.B.** (2014). Numerical simulation of flowing blood cells, *Annual Review of Fluid Mechanics*, 46, 67–95.
- [30] **Jua, M., Yea, S.S., Namgunga, B., Choa, S., Lowa, H.T., Leoa, H.L. and Kim, S.** (2015). A review of numerical methods for red blood cell flow simulation, *Computer Methods in Biomechanics and Biomedical Engineering*, 18, 130–140.
- [31] **Klöppel, T. and Wall, W.A.** (2011). A novel two-layer, coupled finite element approach for modeling the nonlinear elastic and viscoelastic behavior of human erythrocytes, *Biomechanics and Modeling in Mechanobiology*, 10(4), 445–459.
- [32] **Küttler, U., Förster, C. and Wall, W.A.** (2006). A solution for the incompressibility dilemma in partitioned fluid-structure interaction with pure Dirichlet fluid domains, *Computational Mechanics*, 38(4), 417–429.
- [33] **Förster, C., Wall, W.A. and Ramm, E.** (2007). Artificial added mass instabilities in sequential staggered coupling of nonlinear structures and incompressible viscous flows, *Comput. Meth. Appl. Mech. Engrg.*, 196, 1278–1293.
- [34] **Wall, W., Gee, M. and Ramm, E.** (2000). The challenge of a three-dimensional shell formulation—the conditioning problem, *Proceedings of ECCM*.
- [35] **Eken, A. and Sahin, M.** (2016). A parallel monolithic algorithm for the numerical simulation of large-scale fluid structure interaction problems, *International Journal for Numerical Methods in Fluids*, 80(12), 687–714.
- [36] **Eken, A. and Sahin, M.** (2017). A parallel monolithic approach for fluid-structure interaction in a cerebral aneurysm, *Computers and Fluids*, 153, 61–75.
- [37] **Thomas, P.D. and Lombard, C.K.** (1979). Geometric conservation law and its application to flow computations on moving grids, *AIAA Journal*, 17, 1030–1037.
- [38] **Saad, Y.** (1993). A flexible inner-outer preconditioned GMRES algorithm, *SIAM Journal on Scientific Computing*, 14(2), 461–469.
- [39] **Chorin, A.J.** (1968). Numerical solution of the Navier-Stokes equations, *Mathematics of Computation*, 22(104), 745–762.

- [40] **Falgout, R., Baker, A., Chow, E., Henson, V., Hill, E., Jones, J., Kolev, T., Lee, B., Painter, J., Tong, C., Vassilevski, P. and Yang, U.M.**, (2004). Users manual, HYPRE High Performance Preconditioners, UCRL-MA-137155 DR, Center for Applied Scientific Computing, Lawrence Livermore National Laboratory.
- [41] **Balay, S., Abhyankar, S., Adams, M.F., Brown, J., Brune, P., Buschelman, K., Dalcin, L., Eijkhout, V., Gropp, W.D., Kaushik, D., Knepley, M.G., McInnes, L.C., Rupp, K., Smith, B.F., Zampini, S., Zhang, H. and Zhang, H.** (2017). PETSc Users Manual, **Technical Report ANL-95/11 - Revision 3.8**, Argonne National Laboratory, <http://www.mcs.anl.gov/petsc>.
- [42] **Skalak, R., Tozeren, A., Zarda, R. and Chien, S.** (1973). Strain energy function of red blood cell membranes, *Biophysical Journal*, 13(3), 245–264.
- [43] **Flormann, D., Aouane, O., Kaestner, L., Ruloff, C., Misbah, C., Podgorski, T. and Wagner, C.** (2017). The buckling instability of aggregating red blood cells, *Scientific Reports*, 7, 1–8.
- [44] **Hu, X.Q., Salsac, A.V. and Barthés-Biesel, D.** (2012). Flow of a spherical capsule in a pore with circular or square cross-section, *Journal of Fluid Mechanics*, 2012, 176–194.
- [45] **Risso, F., Collé-Paillet, F. and Zagzoule, M.** (2006). Experimental investigation of a bioartificial capsule flowing in a narrow tube, *J. Fluid. Mech.*, 547, 149–173.
- [46] **Barthés-Biesel, D.** (2009). Capsule motion in flow: Deformation and membrane buckling, *Comptes Rendus Physique*, 10, 764–774.
- [47] **Walter, A., Rehage, H. and Leonhard, H.** (2001). Shear induced deformation of microcapsules: shape oscillations and membrane folding, *Colloids and Surfaces*, 183-185, 123–132.
- [48] **Lac, E., Barthes-Biesel, D., Pelekasis, N.A. and Tsamopoulos, J.** (2004). Spherical capsules in three-dimensional unbounded Stokes flows: Effect of the membrane constitutive law and onset of buckling, *Journal of Fluid Mechanics*, 516, 303–334.
- [49] **Yazdani, A. and Bagchi, P.** (2013). Influence of membrane viscosity on capsule dynamics in shear flow, *Journal of Fluid Mechanics*, 718, 569–595.
- [50] **Erzincanli, B. and Sahin, M.** (2013). An arbitrary Lagrangian-Eulerian formulation for solving moving boundary problems with large displacement and rotations, *Journal of Computational Physics*, 255, 660–679.
- [51] **Heil, M.** (2004). An efficient solver for the fully coupled solution of large-displacement fluid-structure interaction problems, *Computer Methods in Applied Mechanics and Engineering*, 193.

- [52] **Deparis, S., Forti, D., Grandperrin, G. and Quarteroni, A.** (2016). FaCSI: A block parallel preconditioner for fluid-structure interaction in hemodynamics, *Journal of Computational Physics*, 327, 700–718.
- [53] **Langer, U. and Yang, H.** (2016). Robust and efficient monolithic fluid-structure-interaction solvers, *International Journal for Numerical Methods in Engineering*, 108, 303–325.
- [54] **Sterck, H.D., Yang, U.M. and Heys, J.J.** (2006). Reducing complexity in parallel algebraic multigrid preconditioners, *SIAM. J. Matrix Anal. & Appl.*, 27, 1019–1039.
- [55] **Baker, A.H., Kolev, T.V. and Yang, U.M.** (2010). Improving algebraic multigrid interpolation operators for linear elasticity problems, *Numerical Linear Algebra with Applications*, 17, 495–517.
- [56] **Karypis, G. and Kumar, V.** (1998). A fast and high quality multilevel scheme for partitioning irregular graphs, *SIAM Journal on Scientific Computing*, 20(1), 359–392.
- [57] **Evans, E. and Fung, Y.C.** (1972). Improved measurements of the erythrocyte geometry, *Microvascular Research*, 4(4), 335–347.
- [58] **Wu, T. and Feng, J.J.** (2013). Simulation of malaria-infected red blood cells in microfluidic channels: Passage and blockage, *Biomicrofluidics*, 7(4), 044115.
- [59] **Heinrich, V., Ritchie, K., Mohandas, N., and Evans, E.** (2001). Elastic thickness compressibility of the red cell membrane, *Biophysical Journal*, 81, 1452–1463.
- [60] **Yoon, Y.Z., Kotar, J., Yoon, G. and Cicuta, P.** (2008). The nonlinear mechanical response of the red blood cell, *Physical Biology*, 5, 036007.
- [61] **Fung, Y.C.** (1981). *Biomechanics - Mechanical Properties of Living Tissue*, Springer Science and Business Media, New York.
- [62] **Sahin, M. and Mohseni, K.** (2009). An arbitrary Lagrangian-Eulerian formulation for the numerical simulation of flow patterns generated by the hydromedusa *Aequorea victoria*, *Journal of Computational Physics*, 228(12), 4588–4605.
- [63] **Shi, X., Zhang, S. and Wang, S.L.** (2014). Numerical simulation of hemodynamic interactions of red blood cells in microcapillary flow, *Journal of Hydrodynamics*, 26, 178–186.
- [64] **Xiong, W. and Zhang, J.** (2010). Shear stress variation induced by red blood cell motion in microvessel, *Annals of Biomedical Engineering*, 38, 2694–2699.
- [65] **Raoult, A.** (1986). Non-polyconvexity of the stored energy function of a Saint Venant-Kirchhoff material, *Aplikace Matematiky*, 6, 417–419.

- [66] **Brighi, B. and Bousseals, M.** (1995). On the rank-one-convexity domain of the Saint Venant-Kirchhoff stored energy function, *Rendiconti del Seminario Matematico della Universita di Padova*, 94, 25–45.
- [67] **Lee, J.S. and Fung, Y.C.** (1969). Modeling experiments of a single red blood cell moving in a capillary blood vessel, *Microvascular Research*, 1, 221–243.
- [68] **Lai, H.S. and Liu, K.L.** (2017). Relationships between the proportional law and the charts used in ASME VII-1 and EN134445-3 for designing shells and tubes under external pressure, *Journal of Pressure Vessel Technology*, 139, 141101–1.
- [69] **Sahin, M. and Wilson, H.J.** (2008). A parallel adaptive unstructured finite volume method for linear stability (normal mode) analysis of viscoelastic fluid flows, *Journal of non-Newtonian Fluid Mechanics*, 155(1), 1–14.
- [70] **Tsukada, K., Sekizuka, E., Oshio, C. and Minamitani, H.** (2001). Direct measurement of erythrocyte deformability in diabetes mellitus with a transparent microchannel capillary model and High-speed video camera system, *Microvascular Research*, 61, 231–239.
- [71] **Blacker, T.D., Benzley, S., Jankovich, S., Kerr, R., Kraftcheck, J., Kerr, R., Knupp, P., Leland, R., Melander, D., Meyers, R., Mitchell, S., Shepard, J., Tautges, T. and White, D.** (1999). CUBIT Mesh Generation Environment Users Manual: Volume 1, **Technical Report**, Sandia National Laboratories, Albuquerque, NM.

CURRICULUM VITAE



Name Surname: Ayşe ÇETİN

Place and Date of Birth: Istanbul, 1992

E-Mail: cetinay@itu.edu.tr

EDUCATION:

- **B.Sc.:** 2016, Istanbul Technical University, Astronautical Engineering

PROFESSIONAL EXPERIENCE:

- 01/09/2016-28/02/2017, R&D Engineer, EDS Hava Uzay Teknolojileri Müh. Lim., Istanbul

PUBLICATIONS, PRESENTATIONS AND PATENTS ON THE THESIS:

- Cetin, A., Sahin, M., 2016. Fluid Structure Interaction Simulation of Red Blood Cells, *VI. Ulusal Havacılık ve Uzay Konferansı*, September 28-30, 2016 Kocaeli, TURKEY.
- Cetin, A., Sahin, M., 2017. A Monolithic Fluid Structure Interaction Algorithm Applied to Red Blood Cells in a Capillary, *47th AIAA Fluid Dynamics Conference and Exhibit*, June 5-9, 2017 Denver, CO, USA.

OTHER PUBLICATIONS, PRESENTATIONS AND PATENTS:

- Cetin A., Bozkus B.S., Ece H.C. Memisoglu O.O., Rodop O., Grate S., Bilgin Y., 2016. Communication Network for Manned Mars Missions, *Poster Presentation, The 4th Mission Idea Contest for Micro/nano Satellite Utilization (MIC4)*, October 21, 2016 Varna, Bulgaria.